

2.1 ZnO: A Multifunctional Material

2.1.1 Crystal Structure

ZnO is a II-VI compound semiconductor which has a room temperature wide bandgap of 3.37 eV (Wang, 2004a). It has high exciton binding energy ~ 60 meV (Klingshirn, 2007), making it as a suitable optoelectronic device candidate (Klingshirn, 2007). ZnO synthesizes in three crystal structure i.e. hexagonal wurtzite, cubic zinc blend and rock salt structures. Hexagonal wurtzite crystal structure is the most stable at room temperature (Ü Özgür et al., 2005a). It contains two closely packed hexagonal sub-lattice of zinc (Zn) and oxygen (O) displaced by $3/8$ along c-axis. The hexagonal wurtzite unit cell of ZnO is presented in figure 2.1 (a). The reported values of lattice constants are $a \sim 3.25$ Å and $c \sim 5.2$ Å. Here, lattice constants, a and c , are related by the fraction $c/a = 1.63$ (Ü Özgür et al., 2005a) (Reeber, 1970). Cubic zinc blend structures are synthesized under special conditions, rock salt is fabricated under high pressure applications and zinc blend is synthesized using epitaxial growth of ZnO on cubic substrate (Ü Özgür et al., 2005a). However, our focus is limited to hexagonal wurtzite structure for the scope of this thesis.

Hexagonal wurtzite structure has $6mm$ point group and $p6_3mc$ space group. Here, one Zn atom is tetrahedrally connected to four O atoms and vice versa. This tetrahedral coordination in wurtzite structure represents sp^3 hybridization (Ü Özgür et al., 2005a). The bonding between Zn and O atom is covalent with partial ionic nature. The small fraction of ionic bonding leads to formation of conduction band minimum (CBM) from $4s$ energy orbitals of Zn^{2+} ions and valence band maximum (VCM) from $2p$ orbitals of O^{2-} ions (Janotti and Van de Walle, 2009) (Ü Özgür et al., 2005a). The splitting in valence band is caused by crystal field and spin orbit splitting (Meyer et al., 2004). The band structure of the wurtzite structure (energy Vs. momentum) is shown in figure 2.1 (b). It has three sub valence bands (A, B and C) and one conduction band. The A and C valence bands have Γ_7 symmetry and B has Γ_9 symmetry (Meyer et al., 2004). The band gap of ZnO is the difference between CBM and VCM of A bands. valence band B is 5 meV below and C is 44 meV below valence band A (Meyer et al., 2004). ZnO has direct band gap as VCM and CBM coincide at Γ point. This direct band gap provides higher luminous efficiency and wide band gap of ZnO makes it more thermally stable. The band gap of ZnO can be further increased (~ 4 eV) or decreased (~ 3 eV) by alloying it with MgO ($E_g \sim 7.8$ eV) and CdO ($E_g \sim 2.3$ eV), respectively (Janotti and Van de Walle, 2009).

Piezoelectricity is generated in ZnO due to the lack of centre of inversion and presence of partial ionic bonding. Hexagonal wurtzite structure has two polar basal planes which are oxygen terminated ($000\bar{1}$) and Zn terminated (0001) along with two non-polar planes along ($\bar{1}000$) (Ü Özgür et al., 2005a). Lack of centre of inversion leads to asymmetry along c-axis and facilitates the growth of anisotropic nanostructures and crystallites of ZnO (Hahn, 2011). The polar basal planes also induce spontaneous polarization due to change

in dipole moments and divergence of surface energy(Hahn, 2011). ZnO has n-type of conductivity and the credit for intrinsic n-conductivity is given to the oxygen vacancies or zinc interstitials however, recently it is reported that these defects act as **deep donors** and does not take part in conduction.

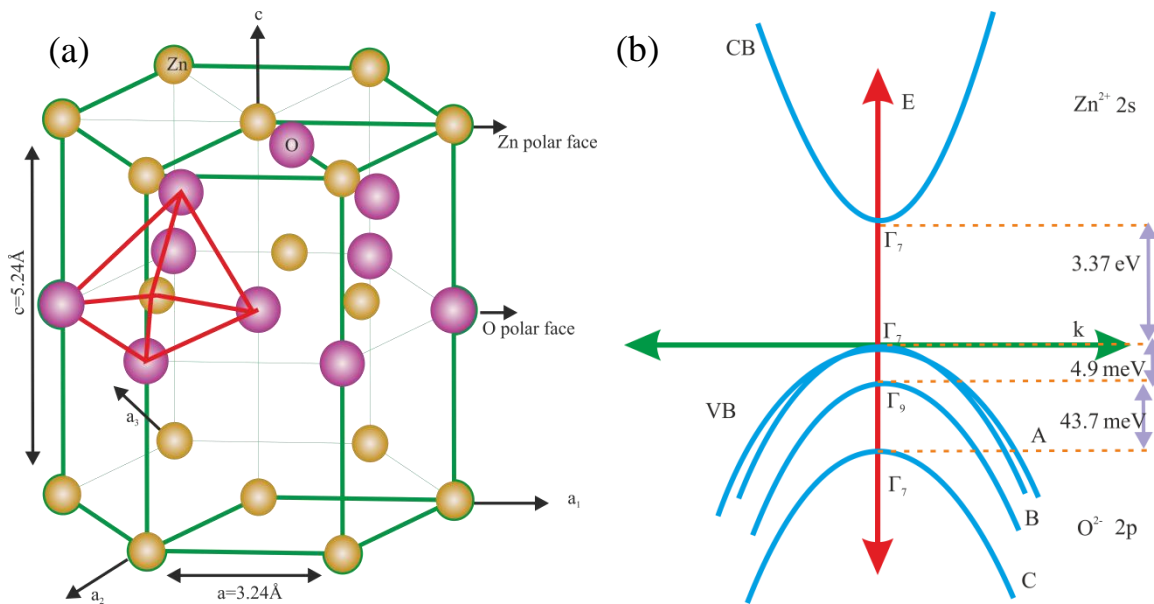


Figure 2.1 : (a) Schematic of crystal structure and (b) Band diagram of ZnO

Density functional theory (DFT) calculations have shown that this intrinsic n-type conductivity is due to availability of unintentional dopants such as hydrogen (Janotti and Van de Walle, 2009). The details of these defects will be discussed in another section of this chapter. The general properties of ZnO are summarized in table 2.1. Here, m_0 is rest mass of electrons/holes in ZnO.

Table 2.1: Physical properties of ZnO semiconductor

Properties	Values
Density	5.606 g/cm ³
Dielectric constant	8.66
Refractive index	2.008
Lattice parameters	a : 3.2495 Å c : 5.2069 Å u : 0.348 c/a : 1.593–1.6035
Thermal expansion coefficient	a_0 : $6.51 \times 10^{-6}/K$ c_0 : $3.02 \times 10^{-6}/K$
Direct band gap energy	3.37 eV
Electron mobility (300 K)	100–200 cm ² /V·s
Hole mobility (300 K)	5–50 cm ² /V·s
Electron effective mass	$0.24m_0$

Hole effective mass	0.59 m_0
Exciton binding energy	60 meV

2.1.2 Mechanical and Electrical Properties of ZnO

Mechanical properties of ZnO such as piezoelectric constant, tensile strength, Young's modulus, hardness, elasticity and stiffness are important and are exploited to be used in different applications. These properties are investigated by several techniques. There exist five elastic constants in hexagonal structure which are C₁₁, C₃₃, C₁₂, C₁₃, and C₄₄ where, C₁₁ and C₃₃ are related to longitudinal mode along the directions [1000] and [0001], respectively (Ü Özgür et al., 2005a). Ultrasonic measurement is considered to be the best to estimate elastic moduli of single crystal ZnO provided the thickness is around ~1 cm (Bateman, 1962). Another technique to find elastic constant and bulk moduli is Brillouin scattering which utilizes the interaction of light with acoustic phonon of the crystal. Techniques such as EDX, angular dispersive X-ray diffraction (ADX) and X-ray absorption spectroscopy (XAS) are explored to understand the influence of pressure on the lattice parameter (Ü Özgür et al., 2005a). Hardness and deformation of ZnO structure is investigated by nano-indentation techniques. The elastic moduli reported by Decremps et al. is ~ 10 GPa which was measured at three different temperatures using ultrasonic wave velocity measurements (Decremps et al., 2002). Bending modulus of ZnO nanobelt is measured up to 50 GPa using an in-situ transmission electron microscopy (TEM) measurements (Bai et al., 2003). The reported elastic constant of ZnO nanowires are 29±8 GPa using AFM technique (Song et al., 2005). The elastic modulus reported for ZnO nanowires along [0001] is in the range of 20-250 GPa. The Young's modulus of bulk ZnO along [0001] is 144 GPa. Size dependent study on nanowires indicated that there is no change in the Young's modulus in 18-304 nm diameter range and the reported value is 133±15 GPa (Wen et al., 2008).

ZnO has intrinsic n-type conductivity which is attributed to the presence of intrinsic defects and unintentional doping of ZnO. The donor ionization energy responsible for n-type doping lies in the range of 10-100 meV and the estimated carrier concentration range of ZnO are 10¹⁵-10¹⁶ /cm³ (Capper et al., 2011). Heavily doped n-type ZnO can have carrier concentration as high as 10²¹ /cm³. ZnO has intrinsic carrier concentration < 10⁶/cm³, mobility of electron is 200 cm²/Vs, electron effective mass is 0.24, maximum n-type carrier concentration is >10²⁰/cm³ and dielectric constant is 8.5. Synthesizing stable p-type ZnO is still a challenging process (Hahn, 2011). This is one of the most challenging problems to extend the optoelectronic devices for application purposes and to synthesize metal-semiconductor junction (ohmic and Schottky) on n & p-type ZnO (Hahn, 2011). However, the fabrication of p-type ZnO is hindered by unavoidable presence of several compensating defects, which are explained in the next section.

2.1.3 Defects

Defects affect the properties of semiconductors. These defects can be intrinsic or extrinsic. Intrinsic defects are attributed to the presence and absence of constituent elements and sometimes presence of unavoidable foreign elements (Janotti and Van de Walle, 2009). The missing of constituent elements forms vacancies, presence of additional constituent elements leads to interstitial defects and presence of one constituent element on another's place originates antisite defects. Hence, point defects such as oxygen vacancies (V_O), zinc vacancies (V_{Zn}), zinc interstitials (Zn_i), oxygen interstitial (O_i) and antisites (Zn_O and O_{Zn}) are present in ZnO lattice (Janotti and Van de Walle, 2007a). These defects act as acceptor or donor and play a crucial role in determining the type of conductivity of ZnO. These point defects influence optical and electronic properties of ZnO and need to be understood in detail. Each

defect is associated with certain formation energy which needs to be provided in order for the defects to be present in the crystal. These defects induce defect energy level in the band gap and also facilitates transition between charge states (Janotti and Van de Walle, 2007a)(Janotti and Van de Walle, 2009). Defect is termed as shallow if it creates a defect level near to VB or CB and if it easily ionizes at room temperature. In contrast to that, deep level defects does not ionise at room temperature and defect energy levels are present in near the middle of CB and VB. apart from that, defects also migrate inside the crystal structure of ZnO which is another reason of compensation for p-type conductivity (Janotti and Van de Walle, 2007a). To understand the migration behaviour, defects are introduced by electronic irradiation or ion implantation and their electronic and magnetic behaviours are studied as a function of temperature. After introducing defects, if the properties change as a function of temperature then it is attributed to migration of that particular defect and further formation energies are calculated by using this information. We will discuss about native point defects in the next section.

2.1.3.1 Native Point Defects

Oxygen vacancies are one of the prominent existing point defects in ZnO. V_O is often reported as the main source of intrinsic n-type conductivity and is attributed to its low formation energy. However, recently DFT calculations revealed that these are deep donor and hence cannot contribute in conduction (Janotti and Van de Walle, 2007a). Neutral charge is assumed by the oxygen vacancy when Fermi level is near to the conduction band in n-type ZnO hence, is not responsible for n-type conductivity. However, in p-type, when Fermi level is above valence band, it has +2 charges with low formation energy and can compensate for p-type conductivity by acting as a donor. Hence, in order to synthesize p-type conductivity, it is necessary to avoid oxygen vacancies and deposition condition should be oxygen rich (Janotti and Van de Walle, 2007a)(Janotti and Van de Walle, 2009).

Zinc vacancies are reported to have high and low formation energies in p-type and n-type ZnO, respectively. Zinc vacancies create four dangling oxygen bonds which form a doubly degenerated state into deep VBM and three degenerated states near to VB. These states have four electrons and further, can occupy two more electrons. Thus, these states contribute in making zinc vacancies acceptors. These vacancies are deep acceptors and increase in formation energy of these defects is observed when it moves toward VCM (Janotti and Van de Walle, 2009)(Janotti and Van de Walle, 2007a).

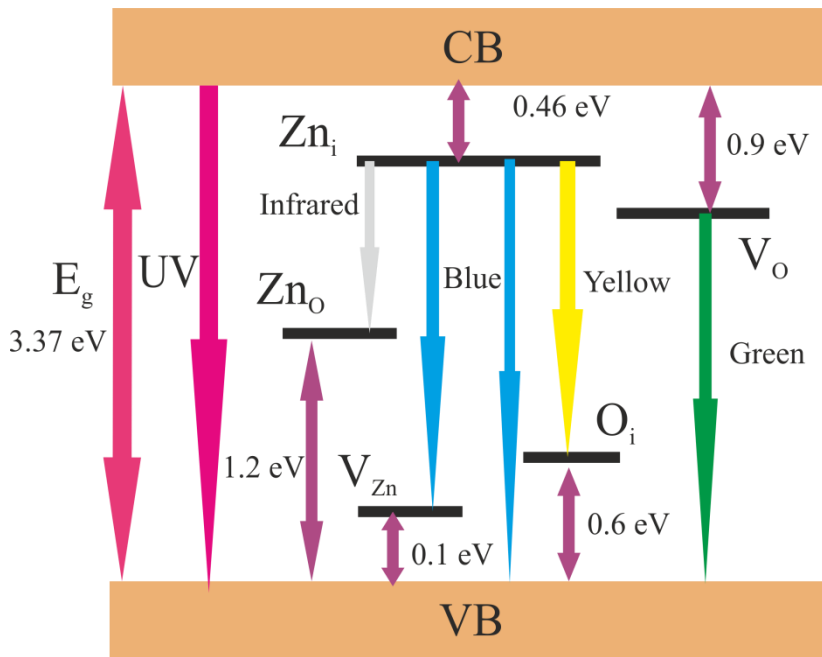


Figure 2.2 : Energy levels of different point defects of ZnO

Zinc interstitials can either occupy tetrahedral or octahedral sites. The tetrahedral site consists of one oxygen and one zinc atom as nearest atoms situated at a distance of 0.88 Zn-O bond lengths. The octahedral site has three oxygen atoms and three zinc atoms as its nearest neighbour at distance 1.07 times the Zn-O bond length. Hence, zinc interstitials are stable in octahedral void and not in tetrahedral. Also, the formation energy of zinc interstitials at tetrahedral site is 0.9 eV higher than that of octahedral sites which facilitates it to occupy octahedral sites. The transition states of Zn_i in different charge states, i.e. from +2 to 0 and +1 to 0, lie above conduction band making it a shallow donor. However, reported formation energy for these defects are higher which makes it to exist in lower concentration, hence its role in n-type conductivity of ZnO is still ambiguous. In contrast to this, when Fermi level is lowering towards VBM for p-type materials then the formation energy lowers which makes it a compensation source of p-type conductivity (Janotti and Van de Walle, 2009)(Janotti and Van de Walle, 2007a).

Zinc antisites have higher energy than previously described defects. It has been reported that it acts as a shallow donor but it is difficult to induce these defects because of its higher formation energy. Similarly, oxygen interstitials and oxygen antisite have higher formation energy in ZnO crystal and cannot be easily introduced. Due to their low concentration availability, these do not play any significant role in the intrinsic conductivity in ZnO material (Janotti and Van de Walle, 2007a)(Janotti and Van de Walle, 2009). The schematic energy band diagram is shown in figure 2.2 explaining different point defects and their respective energy levels.

2.1.3.2 Donor Impurities

The first principle calculations and few experimental results showed that native point defects don't participate in intrinsic conductivity of ZnO. Thus, it is important to understand other defects which might act as donors. The ionic radii of donor and acceptor atoms should be comparable to the host atoms together with similar electronegativity for easy and favourable incorporation of atoms in the lattice. Group III elements act as donors for ZnO. Thus, the common donors are boron (B), aluminium (Al), gallium (Ga) and indium (In) for ZnO system. These donor atoms substitute at zinc site and provide additional electrons. It is reported that Al doping resulted in enhanced donor concentration up to $8 \times 10^{20} / \text{cm}^3$ and the estimated ionisation energy is low $\sim 120 \text{ meV}$ (Zhang et al., 2001). Ga doping has also

improved donor concentration up to 10^{20} without any changes in structural parameters of the film (Ko et al., 2000). Similarly, In has also been proven to be a stable donor in ZnO (Hu and Gordon, 1992). Fluorine as a dopant acts as a shallow donor with low formation energy. The ionisation energy of fluorine in ZnO is ~ 80 meV (Zhang et al., 2001). The fluorine doped ZnO has shown concentration up to $5 \times 10^{20}/\text{cm}^3$ (Hu and Gordon, 1991). Since these materials are not present in ZnO even unintentionally all the time hence, cannot be attributed to the intrinsic n-type conductivity of ZnO.

Hydrogen element has drawn attention as an impurity in ZnO and studied intensively using first principle calculations (Janotti and Van de Walle, 2007b)(Van de Walle, 2000). These studies substantiate that hydrogen interstitials may act as amphoteric dopants for most of the materials indicating that it acts as donor in p-type and as acceptor in n-type (Pankove and Johnson, 1991). Hence, it is considered not to be taking part in prevailed conductivity of those materials. However, for ZnO, it acts as donor in interstitial position (Capper et al., 2011). This interstitial hydrogen can occupy either bond centre (BC) or anti bonding sites and prefers to be near to oxygen to form O-H bonding. However, incorporation of hydrogen in ZnO leads to lattice relaxation, disrupting the position of zinc and oxygen (Capper et al., 2011). Hydrogen also can occupy oxygen atomic site, forming bonds with four nearest zinc atoms. Both interstitial and substitutional hydrogen act as a shallow donor and have low formation energy as well, indicating its presence in ZnO in larger concentration (Capper et al., 2011). It is one of the most possible unintentional impurities which can be the primary source of n-type conductivity in ZnO. Hydrogen can be unintentionally incorporated in ZnO by several deposition techniques such as hydrothermal, vapour phase transport, sputtering and laser ablation. Substitutional hydrogen is demonstrated to be stable up to 500°C and likely to exist more in oxygen deficient condition, substantiating to be one of the reasons for n-type conductivity in ZnO (Shi et al., 2005).

2.1.3.4 Acceptor Impurities

The common acceptors are substitution of group I elements group V elements on Zn and O sites, respectively. The comparable size of ionic radii of lithium to the zinc, makes lithium a suitable acceptor in ZnO (Lander, 1960). Lithium as a dopant in ZnO can act as both donor and acceptor as well. Lithium atoms substituted at Zn site acts as the acceptor and in interstitial positions, it acts as a donor. It has been reported that post annealing after hydrothermal deposition, out diffusion of zinc interstitials, lithium interstitials and hydrogen impurities are initiated resulting in suppressed n-type conductivity (Capper et al., 2011). Copper substitution leads to deep acceptor defect states, yet participates in reducing n-type carrier concentration (Muller, 1976). Nitrogen is one of the widely studied acceptor dopant in ZnO. It acts as an acceptor substituted at oxygen site. Nitrogen doping is realized in ZnO by CVD in the presence of ammonia (NH_3) and calculated ionisation energy is 100 meV (Minegishi et al., 1997). Doping with arsenic (As) and antimony (Sb) are not favourable to achieve p-type conductivity (Capper et al., 2011). Another approach is co-doping method by which p-type conductivity is realized. In co-doping method, acceptors together with donor impurities are introduced or two acceptor impurities are introduced. The incorporation of donor impurities shifts the Fermi level above VBM which reduces the formation energy of acceptors; hence increasing their solubility. It also increases the formation energy of oxygen vacancies by shifting the Fermi energy towards middle of the band gap (Capper et al., 2011). However, presence of donor atom still compensate the acceptors hence such donor atoms are chosen which are easily diffusible after post annealing the samples. Realization of p-type ZnO is reported by co-doping of N and Ga (Joseph et al., 1999). Additionally, isoelectronic impurities such as magnesium (Mg) and cadmium (Cd) has been used for band gap engineering of ZnO, mostly by alloy formation (Janotti and Van de Walle, 2009). Different acceptor atoms and mismatch in their ionic radii are summarized in table 2.2.

Table 2.2 : Different Dopants and Their Ionic Radii (Shannon and Prewitt, 1969)

Element	Ionic Radius (Å)	Mismatch (%) $(r_{\text{dopant}}/r_{\text{host}}-1)$
Zn (+2)	0.60	
Li (+1)	0.59	-2
Na (+1)	0.98	63
P (+3)	0.58	-3
As (+3)	0.60	-0
Sb (+3)	0.76	27
O (-2)	1.38	
N (-3)	1.71	24
P (-3)	2.12	54
As (-3)	2.22	61
Sb (-3)	2.45	78

2.1.4 Optical Properties

Optoelectronics devices utilise semiconductors' characteristics to detect a particular wavelength of light. This light sensing ability of semiconductors depends on band gap of the materials (Sirbuly et al., 2005)(Huang, 2001)(Hoffman et al., 2003). Light source with energy greater than or equals to the band gap energy falls on the materials then electrons and holes are generated in conduction band and valence band, respectively. When the light source is removed, electrons and holes start recombining again, leading to emission of photon energy. This absorption and emission of light source depends on intrinsic as well as extrinsic defects present in the material. These defects create energy states inside the band gap and affect the emission and absorption process (Hahn, 2011). There are number of techniques which are utilized to study these optical properties of ZnO and the widely explored methods are PL, optical absorption/reflection/transmission, cathodoluminescence (CL), Raman spectroscopy and electroluminescence (EL) (Ü Özgür et al., 2005a).

The large band gap of ZnO makes it a suitable light emitter/sensor in ultraviolet (UV) region. Apart from that, ZnO has several other intrinsic and extrinsic defects present, allowing light emission in visible region. ZnO shows two emission peaks, one is centred at ~ 376 nm and is termed near band edge emission (NBE) and is a characteristics of recombination of free exciton participating in transition (Djurišić et al., 2010a)(Djurišić and Leung, 2006). The exception to NBE is the presence of A-line near 381 nm which is reported in ZnO nanostructures with high surface to volume ratio (SVR) and the exact explanation of this behaviour is still a matter of debate (Schneider et al., 2007)(Djurišić et al., 2010a)(Wagner et al., 2011). The other peak lies in visible region and is attributed to defects such as V_{O} , Zn_{i} , O_{i} , V_{Zn} , antisites and foreign surface adsorbed group (Djurišić et al., 2010a). The defects related transition ranges in entire visible region from violet to red. The source of these defects related transition and assigned wavelength are still a matter of debate and has been reported to also dependent on size, shape, deposition condition and deposition techniques of ZnO (Djurišić et al., 2010a)(Djurišić and Leung, 2006)(Kurbanov et al., 2007). The transition wavelength in violet to blue (400-488 nm) is particularly assigned to the presence of zinc interstitial defects which acts as shallow donor and combines with holes in valence band (Zeng et al., 2010)(Xue et al., 2002). This transition is sometimes also attributed to coupling of defects in disordered lattice or transition of zinc interstitials defects to zinc vacancies (Zeng et al., 2010)(Ahn et al., 2009). The reported emissions of these defects levels are low because zinc interstitials are said to be unsteady at room temperature, hence does not exist in large

number (Zeng et al., 2010). The green (497-564 nm) region transition energies are attributed to several recombination mechanisms and the most common among them is radiative recombination at oxygen vacancies defect states (L. Zhang et al., 2010)(Norberg and Gamelin, 2005). The relative intensity of this energy level depends on the density of different defect states acting as recombination centres and it largely depends on the type and parameters of deposition techniques. In nanostructures with large SVR, this region is attributed to presence of OH group, inherently adsorbed on the surface (L. Zhang et al., 2010)(Norberg and Gamelin, 2005). There have been several other mechanisms explaining the green emission which are transition between V_O (donor) and V_{Zn} (acceptor), O_i and antisite (Guo et al., 2003)(Lin et al., 2001). Yellow to red (576-600 nm) is observed in oxygen rich condition and is attributed to O_i (Wu et al., 2001). Similarly orange to red emission is also attributed to O_i along with presence of Zn_i and complexes of V_{Zn} (Ahn et al., 2009). However, the exact mechanism of these emissions is still not clear and more research is needed for detail understanding.

2.1.5 Deposition Techniques

There are numerous techniques to deposit ZnO films and nanostructures. The various defects present in ZnO system depend on growth techniques as well so understanding these methods are important. Deposition techniques are categorized into three types i) chemical vapour deposition (CVD), ii) physical vapour deposited (PVD) and iii) solution process. Chemical vapour methods include deposition techniques such as thermal CVD, molecular beam epitaxy (MBE), plasma enhanced CVD (PECVD), metal organic CVD (MOCVD) and atomic layer deposition (ALD). The examples of PVD methods are sputtering, thermal evaporation, and pulsed laser deposition (PLD). Solution processes contains hydrothermal and sol-gel techniques. Advantages and disadvantages of these systems are given in table 2.3.

2.1.5.1 Thermal Evaporation

Thermal evaporation system comprises of a vacuum chamber where source and substrate materials are placed. The base pressure is in the range of 10^{-6} - 10^{-7} Torr, while working pressure is maintained around 10^{-2} - 10^{-3} Torr. The source is placed inside the crucible, the chamber is evacuated first up to a desired base pressure and then the source material is heated using a heating element. The heating temperature is kept below its vapour point for material to evaporate and thus, deposit on substrate. The heating source may be electron beam, radio frequency (RF) inductive, and/or resistive heating. In electron beam heating, an electron beam is allowed to fall on the source which sublimates it. In RF inductive heating, the alternating current (AC) is produced by an AC supply. This supply current generates magnetic field and the source placed in this magnetic field generates eddy currents. These eddy currents generate localized heating, sufficient to evaporate the material. The higher frequency leads to higher deposition rates. In resistive heating, resistive elements such as tungsten or molybdenum are used to generate heat. The electron beam and RF inductive heating are used to deposit high quality thin film of various metals and metal oxides, whereas resistive heating is used mainly to deposit metallic thin films. However, there are some reports where thermal evaporation is also used to deposit variety of nanostructures of different shapes of ZnO (Agarwal et al., 2006)(Wang, 2005)(Z. L. Wang et al., 2004).

2.1.5.2 RF/DC Sputtering

Sputtering is a technique in which atoms are removed from the source by momentum transfer from the ionizing atoms and is deposited on the substrate. There are different techniques of atom removal from the target, which are focus beam, direct current (DC), RF and magnetron sputtering methods. In focus beam technique, gallium ions are accelerated and moved in vacuum chamber towards the target. Gallium has low melting temperature as

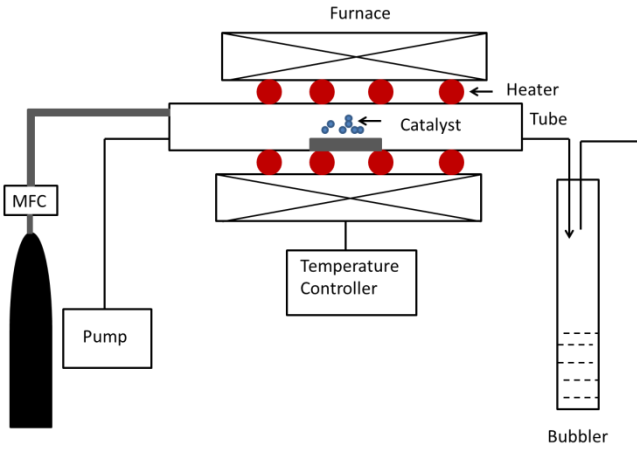
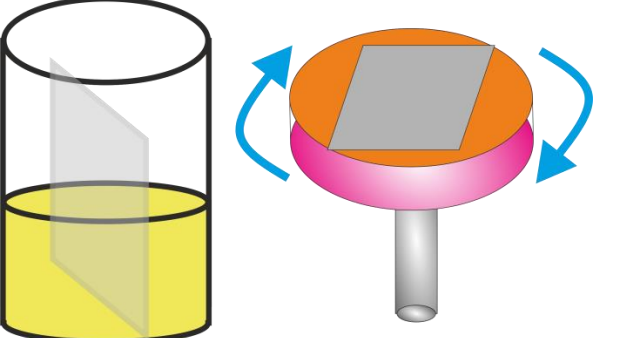
well as low vapor pressure which makes it a well handled work source and ensures high evaporation. The acceleration and focussing is done by a series of capacitive plates and magnetic coils, respectively. In sputtering, target and substrate are placed inside the vacuum chamber. The chamber is vacuumed and an inert gas such as argon is released in the chamber. The DC power supply is used to ionise this gas and the gas ions collide/impact with target and removing target atoms. These removed atoms are deposited on the surface. The disadvantage of DC sputtering is the requirement of very high voltage for insulating targets. To overcome the same, RF sputtering is used which uses AC power which charges and discharges the target after each half cycle. Apart from that, in magnetron sputtering, a magnetic field is used to concentrate the plasma near the target, which increases the deposition rate, especially for insulating materials. Sputtering techniques is used to synthesize polycrystalline thin films and nanostructures. Schematic of sputtering system is shown in table 2.3.

2.1.5.3 Pulsed Laser Deposition (PLD)

In PLD, a vacuum chamber consists of laser source with high flux density and short pulses which is focused on the target material. Thus, the target material is heated and when the temperature of the source is near to the evaporation temperature, a vapour plume is formed. This plume has the same stoichiometry as the target material, which is deposited on the substrate. Single crystal substrates facilitate the formation of single crystal epitaxial films using this method. This method has produced numerous binary and ternary epitaxial thin films together with nanorods and nanodots without any catalyst (Sun et al., 2004)(Nakamura et al., 2002)(Bae et al., 2006).

Table 2.3 Advantage and Disadvantage of Different Deposition Techniques

Deposition techniques	Advantages	Disadvantages	
PVD	Wide range of coating, good adherence, crystalline and defect free film synthesis, uniform film	High vacuum, yield is low, line of sight requirement between source and substrate, high cost	

CVD	Wide morphology, high deposition rates, no high vacuum	High temperature, may contain cracks, volatile precursors requirement, precursors may be corrosive and hazardous	 <p style="text-align: center;">Thermal CVD system</p>
Solution process	Low temperature, no vacuum, low cost, different morphology	Difficult to control composition, scalability issue, difficulty in controlling particle size and uniformity, non-uniformity problem	 <p style="text-align: center;">CBD and spin coating</p>

2.1.5.4 Chemical Vapor Deposition (CVD)

In CVD, a source material is placed inside a tube, where pressure and flow of a facilitating gas is controlled in order to realize the deposition. During thermal CVD, a pressure of 10^{-3} Torr or lower is created to ensure that the residual gases are removed and then a reactive or inert gas is introduced in the tube. The source material is placed at a higher temperature (near to the materials' vaporising temperature) and the substrate is placed at lower temperature zone of the tube. The source zone is at higher pressure and temperature zone and the substrate is at lower pressure and temperature zone. Thus, the source material moves towards the substrate with the help of inert gas or reactive gas together with reacting with the reactive gas. The source material is settled on the lower temperature zone where substrate is kept and facilitates the growth. It has been categorized into (i) vapour-liquid-solid growth (VLS) and (ii) vapour-solid growth (VS). In VLS growth, generally a catalyst is required on the substrate, which facilitates the growth of different nanostructures. Generally metal catalyst is deposited on the substrate for creating nucleation sites on heating. When semiconducting materials deposit in these nucleation sites, it makes a metal-semiconductor alloy. Further, deposition of semiconductor oxides leads to saturation and facilitating the growth of different nanostructures. Where as in VS, deposition takes place without any catalyst. Here, the source material deposited on the substrate acts as nucleation site leading to the synthesis of different nanostructures (Schmidt-Mende and MacManus-Driscoll, 2007b). There are several ZnO nanostructures fabricated by this technique (Schmidt-Mende and MacManus-Driscoll, 2007b). This technique generally requires high temperature for deposition and is suitable for the growth of ZnO nanostructures. This is one of the techniques, used in this dissertation for the deposition of ZnO nanostructures. Plasma enhanced CVD (PECVD) relatively needs lower temperature than thermal CVD and plasma is generated inside the tube to facilitate the growth. MOCVD uses metal organic precursors

for ZnO growth and have been used to deposit nanowires, nanotips, nanotubes and thin films of ZnO (Schmidt-Mende and MacManus-Driscoll, 2007b). A schematic of CVD system is shown in table 2.3.

2.1.5.5 Molecular Beam Epitaxy (MBE)

MBE utilises an ultra-high vacuum chamber. Pure materials in atomic/molecular forms are transported in the deposition chamber by heating materials in quasi-Knudsen cells to produce vapours. These vapours are introduced in the chamber to the substrate by using a computer controlled shutter. Epitaxial films are grown layer by layer upon exposing to single crystal substrates. Reflective high energy electron diffraction (RHEED) is used to monitor thickness of the film as well as crystalline quality. This technique has been used to deposit ZnO single crystal as well as quantum dots because of the precise control of the process (Fonoberov and Balandin, 2004)(Nakahara et al., 2001).

2.1.5.6 Atomic Layer Deposition (ALD)

ALD is a self-limiting surface controlled deposition technique where layer by layer controlled deposition of thin film takes place. Here, the deposition of each precursor takes place in one half preventing the precursors to react with each other. The main advantage of ALD is its capability to deposit high quality thin films at relatively lower temperatures, suitable for device applications (Tynell and Karppinen, 2014).

2.1.5.7 Solution Process

Solution method generally required a liquid environment to facilitate the growth of the desired material. Solution processed materials have high uniformity and good yield but it suffers from high point, line, and planar defects as compared to other techniques. Hydrothermal method uses water as a solvent at elevated conditions. The small crystals come out of the solution at higher temperature and pressure and nucleate on the substrate. The autoclave and bomb makes water supercritical, which enhances the dissolving capacity, mass transport, and diffusivity by reducing the viscosity of the solution. The density of the deposited material can also be controlled by tuning the pressure. The seed layer assisted synthesis of ZnO nanostructures is favourable because it acts as nucleation point and facilitates the growth of highly oriented nanorods. The most commonly used precursor materials are zinc nitrate and hexamethylenetetramine (HMTA). The uses of other zinc salts such as zinc acetate dihydrate and zinc chloride are also reported. However, the use of nitrate and chlorate precursors leads to the retention of anion species in final product which makes zinc acetate a good candidate to synthesize ZnO nanostructures. The role of HMTA is still under debate. Here, Zn^{2+} and O^{2-} are originated from zinc nitrate and H_2O molecule respectively. HMTA is reported to be a source of OH^- ions by decomposing into formaldehyde and ammonia, a source of pH buffer and as nonpolar chelating agents to facilitate the growth along c-axis (Govender et al., 2004)(Ashfold et al., 2007)(Sugunan et al., 2006). The growth conditions using zinc nitrate and HMTA is summarized below (Schmidt-Mende and MacManus-Driscoll, 2007b).

Decomposition: $(CH_2)_6N_4 + 6H_2O \leftrightarrow 6HCHO + 4NH_3$

Hydroxyl supply: $NH_3 + H_2O \leftrightarrow NH_4^+ + OH^-$

Supersaturation: $2OH^- + Zn^{2+} \rightarrow Zn(OH)_2$

Final reaction: $Zn(OH)_2 \rightarrow ZnO(s) + H_2O$

Supersaturation reaction plays important role in synthesis of ZnO. Large number of hydroxyl ions produced in short time will lead to quick precipitation of Zn^{2+} ions facilitating homogeneous nucleation which is not favourable (Govender et al., 2004). The hydrothermal growth can be controlled by controlling the seed layer, precursor type, time, pressure,

temperature and pH of the solution. Synthesized ZnO from hydrothermal method are of high quality and of different morphologies (Schmidt-Mende and MacManus-Driscoll, 2007b). Sol gel method is another technique which uses inorganic salts of the materials as a solute and a solvent. First, a colloidal solution is formed between solute and solvent and then the gelation of the solution is done for further conversion into gel. This gel is spin coated on the substrates to get the desired structures. ZnO films, nanorods and crystals have been synthesized by using this method (J. Wang et al., 2007)(Ahn et al., 2004). Schematic of spin coating technique is listed in table 2.3.

Electrodeposition is another method which is used to deposit ZnO thin films and nanostructures. It consists of an electrolyte solution made of zinc salts along with a reference, counter and working electrodes. Applied electric field causes the ions to migrate and to be deposited on the substrate. The growth rate offered by electrochemical deposition is faster but that demands a conducting substrate which imposes the limitation on this deposition technique (Schmidt-Mende and MacManus-Driscoll, 2007b). All these growth solutions are used to realize different nanostructures of ZnO and few of them are described in the next section.

2.1.6 Nanostructures

Nanostructures have different electronic and surface properties than bulk or thin films. Large surface to volume ratio of nanostructures have more surface atoms exposed which indeed affects the electronic properties of materials. ZnO exhibits large number of nanostructures synthesized by different techniques hence, understanding the growth of different nanostructures are important.

ZnO nanorods and nanowires have been synthesized by a number of techniques such as CVD, PVD and hydrothermal techniques. CVD based VLS method is one of the largely explored techniques to synthesize nanorods and nanowires. This technique requires a catalyst which is chosen in such a way that the source materials are soluble in liquid form but does not form a stable solid compound with this catalyst metal (Zhang et al., 2012). The source material is kept in a higher temperature zone (500-1100°C) and substrate is kept at lower temperature zone which is higher than the eutectic point of the catalyst used (Djurišić et al., 2010b). The catalyst liquid droplets act as the absorption sites for the source materials. When the droplet is supersaturated, then nucleation starts and growth of nanorods/nanowire is facilitated. Growth continues till the droplet is in liquid form and the precursors are available. The catalyst governs the growth direction and the diameter of the nanorods. After the final growth, catalyst nanoparticle is present at the top or bottom of nanorods (Djurišić et al., 2010b). The different metal catalysts used are Au, Cu, Ni and Sn etc. Carbothermal is a type of CVD technique which used the combination of ZnO and carbon to reduce the vaporization temperature of ZnO which is very high (~1900 °C). This technique has been used widely for deposition of nanorods and other nanostructures. ZnO nanowires are grown on Sapphire, AlGa_N, GaN, and AlN substrate using VLS process (Wang et al., 2005). The nanowire growth depends on chamber pressure, partial pressure of oxygen, catalyst thickness and amount of reactants. ZnO nanowires are grown on Si substrate in temperature range 600-950°C and pressure in the range of 0.75-3 Torr. Highly aligned ZnO nanorods are grown using this technique with high aspect ratio in 700-750 °C and above 800°C, and a decrease in the density of nanorods is observed. Further, it is also noticed that the increase in chamber pressure led to the reduced growth rate and length of nanowires (Chu et al., 2012). Also, the presence of metal nanoparticles at the nanorods/semiconductor interface affects the optoelectronic properties which may not be desirable sometimes(Djurišić et al., 2010b). Hence, recently focus has been shifted on VS technique. The growth of highly aligned defect free nanorods have been demonstrated using carbothermal VS method, by using PLD deposited ZnO seed layer as a starting material (Jie et

al., 2005). MOCVD has been also used to grow nanorods which uses low temperature and requires no catalyst in comparison to VLS technique. High quality ZnO nanowire is prepared by using diethyl zinc as zinc source and N₂O as oxygen source in the presence of N₂ carrier gas. Thin ZnO seed layer is first prepared at lower temperature (400 °C) and growth of nanowires is facilitated at higher temperature ~650 °C (Zeng et al., 2005). Thermal evaporation is also used to synthesize ZnO nanowires. ZnO nanowire is grown on Si substrate by using zinc as source material. This zinc is evaporated at 500 °C in the presence of N₂ gas flow (50 cm³/m) and at a pressure of 10⁻³ torr for one hour (Zhang et al., 2009). The obtained nanowires are of high quality and substantiate better optical properties.

The other important methods are hydrothermal, CBD, and solvothermal, commonly used to synthesize nanorods and nanowires. In hydrothermal method, water is used as the solvent while in solvothermal method, another solvent such as alcohol is used. Growth of nanorods via solvothermal is rare as it needs higher temperature to facilitate the growth. The seed layer coated substrates are submerged in the solvent at certain temperature for a time period for realization of nanorods in hydrothermal and CBT methods. The thickness, texture and crystallite size of ZnO seed layer have major effect on the growth mechanism of nanorods (Zhang et al., 2012). It is reported that with increasing seed layer thickness from 20-100 nm, the diameter increases from 50-130 nm, density of nanorods decreases from 110-60 μm⁻², and length also decreases (Ji et al., 2009). Different alkaline reagents such as HMTA, NaOH, Na₂CO₃, NH₃ and ethylenediamine are used as a source of OH⁻ ions. NaOH, KOH and Na₂CO₃ need high temperature (>100°C) and also to be kept in hydrothermal autoclave at higher pressure. In contrast, HMTA and ethylenediamine reagents need relatively lower temperature and even atmospheric pressure is sufficient to produce OH⁻ ions (Zhang et al., 2012). Different precursor concentrations also affect the density and diameter of the nanorods. Some reports show that the increase in concentration from 8 mM -40 mM increased the diameter from 43-70 nm and also the length from 65 nm to 320 nm (Wang et al., 2008). The time duration also affects the growth diameter and length. However, the growth decreases after certain duration due to the depletion of the precursors.

ZnO based nanobelts are also realized with exposed side surfaces. This has been reported that nanobelts are synthesized by sublimating zinc powder (Pan et al., 2001). Width and thickness are reported to be in the range of 50-300 nm and 10-30 nm, respectively. The length of nanobelt grows along [01 $\bar{1}$ 0], top and bottom surfaces grow along ±(2 $\bar{1}$ $\bar{1}$ 0) and side surfaces along ±(0001) plane directions (Wang, 2004b). Ultra-narrow nanobelts of ZnO are reported by using tin (Sn) thin film as catalyst on Si substrate. Length of nanobelts are along [0001], top surfaces along (2110) and their side surfaces along (0110) directions. The estimated average diameter is 5.5 nm and the standard deviation is ±1.5 nm, indicating good size uniformity (Wang, 2004a).

Nanocombs and nanosaws are other ZnO nanostructures which have been reported. The synthesized combs showed growth in length along (0001), top and bottom surfaces are grown along (01 $\bar{1}$ 0) direction and side surface along (2 $\bar{1}$ $\bar{1}$ 0) direction. It is deduced that positively charged Zn (0001) surface and negatively charged O (000 $\bar{1}$) are chemically active and inert, respectively, which supports the growth along (0001) forming long fingers resulting in ZnO nanocombs (Wang, 2004a)(Wang, 2004b). Another type of nanostructures is nanopyramids, nanosprings and nanospirals. Surface energies of (0001), (01 $\bar{1}$ 0) and (2 $\bar{1}$ $\bar{1}$ 0) planes are different hence, formation of nanobelts along non-polar (01 $\bar{1}$ 0) and (2 $\bar{1}$ $\bar{1}$ 0) surfaces are favourable due to their lower formation energy. Recently by introducing Li and In as impurity elements, in ZnO, nanobelts along (0001) direction has been synthesized which shows spiral and spring morphology. The nanobelt length grows along (2 $\bar{1}$ $\bar{1}$ 0) while top and bottom large surface along ± (0001) and the side surfaces grew along ± (01 $\bar{1}$ 0). The estimated thickness and aspect ratio is of

5-20 nm and ~1:4, respectively, which make it highly flexible. Due to reduction in electrostatic energy, a spiral structure formation takes place (Wang, 2004a)(Wang, 2004b). Nanorings are synthesized by using In as impurity in ZnO. The reported thickness of the ring is 10 nm with large radius. The nanoring formation takes place due to unsaturated charges which induces electrostatic energy due to dipole moment; the folding of charged surface reduces the overall electrostatic energy making it stable (Wang, 2004a)(Wang, 2004b). By adjusting the source material such as ZnO and SnO₂ in ratio 1:1, nanopropeller like structure of ZnO is realized using VLS method. Self-assembly process is used to synthesize ZnO based cages and shell structure by epitaxial surface oxidation of the film (Wang, 2004b).

2.1.7 Devices

2.1.7.1 Gas Sensors

ZnO is widely investigated for its different gas sensing abilities. The conductivity of ZnO surface changes by adsorption or desorption of gas molecules on its surface. Oxygen molecule present in the atmosphere is adsorbed on ZnO surface and converts it into oxygen ion. Due to that, the surface electrons in ZnO are depleted. In presence of reducing gases, the electron is supplied back to surface which leads to decrease in resistance. Oxidising gases further takes the electron from surface and tends to increase the resistance. Different thin film and nanostructures of ZnO are investigated for gas sensing applications. 1-D ZnO has attracted wide attention for gas sensing properties because of its high surface to volume ratio. ZnO based gas sensors are reported to be operated at room temperature or elevated temperature. The room temperature operation is preferred because it is beneficial in detecting explosive gases, which also reduces energy consumption and doesn't degrade sensor performance with time (Zhu and Zeng, 2017). These gas sensors are fabricated in simple chemiresistive configuration and FET configuration. FET configuration provides the additional advantage of manipulating the source to drain voltage which tends to increase selectivity and sensitivity of such devices (Zhu and Zeng, 2017). There are several gases which are sensed by ZnO such as NO, NO₂, NH₃, CO, H₂ and H₂S (Zhang et al., 2012). The selectivity and sensitivity of ZnO based gas sensors are improved by applying surface decoratives, metal doping, and by using its selective polymer composites (Zhu and Zeng, 2017). The sensitivity of devices is also increased by light activation i.e. using ultraviolet and visible light sources which enhances the number of holes which recombines with adsorbed oxygen molecule facilitating its desorption (Zhu and Zeng, 2017). Oh et al. synthesized ZnO nanorods based NO₂ gas sensor on platinum patterned alumina substrate by using a sonication method. The reported detection limit is very low up to 10 ppb at 250 °C, showing high sensitivity (Oh et al., 2009). NH₃ gas detection is reported by Wei et al. on Au patterned electrode on hydrothermally synthesized nanorods (Wei et al., 2011). Oh and Jeong reported CO gas sensors based on hydrothermally grown nanorods which shows small detection limit for 1 ppm at 350 °C (Oh and Jeong, 2011).

2.1.7.2 Biosensors

ZnO based nanostructures are one of the best candidates for biosensing applications owing to its non-toxicity, high electron transfer rate, bio-compatibility and ability to combine with enzymes. ZnO has high isoelectric point (IEP) which makes it a suitable matrix to immobilize low IEP DNA or acidic proteins. High ionic bonding content of ZnO make it less soluble in normal pH conditions (Zhang et al., 2012). Several nanostructures of ZnO have been investigated for detection of glucose. Bio sensors can be both enzymatic and non-enzymatic; however, non-enzymatic biosensors are needed to have stability and to reduce the complexity and cost of the device. Lie et al. fabricated a ZnO nanorods based amperometric glucose sensor. The sensor indicated linear response to 5-300 μM concentration with a 3 μM limit of detection. This device indicated excellent selectivity in the presence of uric acid and ascorbic acid (X. Liu et

al., 2009). Bupoto et al. fabricated ZnO nanorods based enzymatic penicillin sensor by using penicillinase as enzyme. The observed linearity range was from 100 μ M-100 mM (Ibupoto et al., 2011). Apart from these, several other bio materials such as H₂O₂, phenol and cholesterol has been sensed by ZnO nanostructures (Zhao et al., 2010).

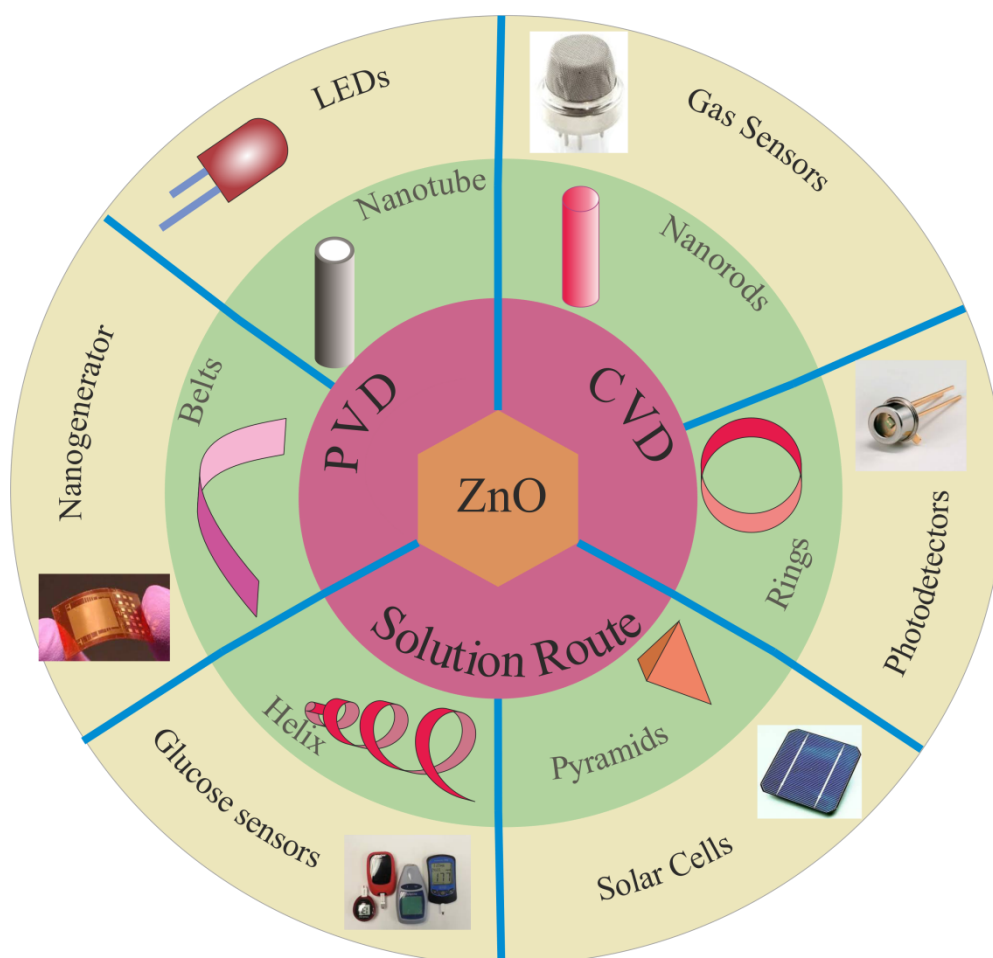


Figure 2.3: Schematic of ZnO structures and their applications in different fields of engineering and technology.

2.1.7.3 Solar Cells

Dye sensitized solar cells (DSSC) are a good substitute of silicon based solar cell as these are flexible, inexpensive and easy to fabricate (Zhang et al., 2012). The disadvantages associated with DSSCs are that it suffers from dye agglomeration and electrolyte leakage. These solar cells are combination of MOS and complex dyes of organic /metal organic systems. ZnO is considered one of the promising materials for solar cell applications because of its fast electron transport with reduce recombination losses, ease of crystallization and growth techniques (Zhang et al., 2012). High surface to volume ratio of 1-D ZnO nanostructures provides more dye loading area which improves the efficiency. Ko et al. investigated the DSSCs properties on well aligned and branched nanowires samples. They reported that efficiency of branched nanowires are better than that of length wise grown nanowires (Ko et al., 2011). Lupan et al. reported the effect of vertically aligned nanowires deposited on ITO coated glass substrate using electrodeposition method. The reported maximum conversion efficiency was 0.66 % under applied flux of 100 mW/cm² (Lupan et al., 2010). Cheng et al. reported branched like ZnO nanowires solar cell, deposited on conducting glass and the calculated efficiency was 1.51% at 4.27 mA/cm² current density (Cheng et al., 2008). Higher conversion efficiency of 1.82 % is reported by Sudhagar et al. with jack like ZnO nanorods and used as a photoanode in DSSC.

They also compared it with branch free nanorods with conversion efficiency around 1.08 % (Sudhagar et al., 2011).

2.1.7.4 Piezoelectric Devices

ZnO exhibits a piezoelectric behaviour because of existing non-centrosymmetric characteristics of hexagonal wurtzite structure (Zhang et al., 2012). ZnO based nanogenerators are developed on nanowires by using air flow and body movements as source of mechanical forces. Zhu et al. reported a flexible nanogenerator using lateral ZnO nanowires to drive a small electronic component. The generated energy efficiency was 4.6 % and it was used successfully to light a LED (Zhu et al., 2010). Hu et al. used ZnO based nanogenerator on tyres of automobiles to generate energy. The energy produced in deformation of tires are supplied to a liquid crystal display (LCD) (Hu et al., 2011). Hybrid cell based on nanogenerator and DSSC are reported to have increased output power (Xu and Wang, 2011). Sound based piezoelectric nanogenerator was fabricated by Cha et al. using ZnO nanostructures and the reported AC output voltage was 50 mV (Cha et al., 2010). The high frequency surface acoustic wave (SAW) capabilities of ZnO have been explored by depositing it on high acoustic velocity substrates such as aluminium nitride (AlN) and silicon carbide (SiC). ZnO thin film (400 nm) deposited on SiC substrate showed normal SAW modes and pseudo SAW mode with acoustic velocity 7000 m/s and 12500 m/s, respectively (Didenko and Hickernell, 2000).

2.1.7.5 Light Emitting Devices (LEDs)

High exciton binding energy of ZnO makes it one of the interesting candidates for LEDs applications. First ZnO based heterojunction LED was synthesized by Drapak in 1968 where p-type layer was Cu₂O (Özgür et al., 2010b). Several heterojunction ZnO based LEDs are fabricated but these devices suffers from high lattice mismatch and hence shows less efficiency due to several defects present at the interface. A variety of organic and inorganic p-type materials are investigated for ZnO based heterojunction. LED characteristics of n-ZnO nanorods/p-CuAlO₂/p-Si and n-ZnO nanorods /p-Si have been studied (Djurišić et al., 2010b). Nanorods were deposited using thermal deposition technique on a predeposited ZnO seed layer. Gaps between ZnO nanorods were filled by using PMMA. The devices showed good rectification behaviour. Emission spectra of CuAlO₂ device showed strong emission in UV range and week emission in visible range and p-Si based device showed week emission in UV range (Djurišić et al., 2010b). LED devices based on ZnO nanorods and p-Si and p-poly (3,4-ethylene-dioxythiophene):poly(styrene sulfonate) (PEDOT:PSS) have also been reported. The devices showed good rectification behaviour and devices based on p-Si exhibits emission in visible and NIR region, where as PEDOT:PSS device showed emission in UV region (Djurišić et al., 2010b). p-type GaN is one of the most explored materials for heterojunction LED synthesis with ZnO because of its small lattice mismatch with ZnO (Djurišić et al., 2010b). Homojunction ZnO LEDs are difficult to fabricate because of the difficulties on synthesising stable p-type ZnO. The lattice matching in homojunction devices exhibits better luminescence properties because of lesser interface defects and hence, homojunctions devices are preferred over heterojunction devices. Various efforts are put to synthesize p-ZnO to realize homojunction based LEDs. LED device based on phosphorous doped p-ZnO and gallium doped n-ZnO on sapphire substrate, prepared using RF sputtering is reported. The device showed UV emission along with a broad emission in visible range. Insertion of 40 nm thick Mg_{0.1}Zn_{0.9}O and ZnO layer between the junctions led to suppression of visible emission and enhancement of UV emission (Lim et al., 2006). Further, arsenic doped p-type BeZnO alloy and gallium doped n-type ZnO thin film deposited by hybrid beam deposition based LED structures are investigated intensively. The estimated turn on voltage is ~ 10 V and the room temperature electroluminescence (EL) was observed at 363 and 388 nm (Ryu et al., 2006). N-In co-doped p-ZnO and n-ZnO thin film on GaAs substrate based LEDs are also reported. The devices showed a turn on voltage ~ 4V (Du et al., 2006).

2.1.7.6 UV Detectors

The wide band gap of ZnO which lies in UV region makes it an interesting candidate for visible blind UV detector. Various devices are reported on ZnO nanostructures based UV detectors. Chen et al. synthesized ZnO nanowire based UV detector with IrO₂ electrode. They reported that the photogenerated current is 5.11×10^{-7} A under 5V bias voltage and is two times higher than the dark current (K. J. Chen et al., 2009). Yang et al. fabricated self-assembled lateral growth of ZnO nanowires. They reported that the photogenerated current is twice in comparison to dark under 5V bias voltages (Yang et al., 2010). p-Si and n-ZnO nanorods based UV detector is also reported and the reported rise and decay time was 360 and 280 ms, respectively (Djurišić et al., 2010b). ZnO nanoflake and nanowire, synthesized by oxidizing zinc, showed small rise and decay time constants 20.35 and 3.9 ms, respectively (Djurišić et al., 2010b).

2.1.7.7 Other Devices

ZnO has been also used in phot catalysis. Baruah et al. reported that ZnO nanowires synthesized on woven polyethylene is suitable to degrade methylene blue under UV exposer (Baruah et al., 2008). ZnO is also used to synthesis thin film transistor (TFT) and transparent TFT (TTFT) as channel layer. Indium doped ZnO has been fabricated by RF sputtering and AlO_x layer has been used as gate dielectric for TTFT application (Song et al., 2007). The device showed low threshold voltage ~ 1.1 V with high on/off ratio $\sim 10^6$, saturation current 1.41 μ A at 5 V and $\sim 80\%$ transmittance. ZnO is also used in lithium ion batteries, RRAM devices and cantilevers (Özgür et al., 2010b)(Djurišić et al., 2010b).

2.2 BiFeO₃: A Multifunctional Multiferroic System

2.2.1 Crystal Structure and General Information

BFO is a perovskite material and belong to the class which is represented by the formula ABO₃ where A, and B are cations of different valence and O is anion. It has R₃C space group and possess rhombohedral structure in which two perovskite unit cells are connected along the body diagonal. The lattice constants are $a=3.96 \text{ \AA}$ and $\alpha=89.45^\circ$ with ferroelectric polarization along [111] plane at room temperature (Catalan and Scott, 2009). It consists of FeO₆ octahedron centred at Fe atom and surrounded by 6 oxygen atoms. The tilting angle of the octahedron is $\sim 11^\circ$ (Catalan and Scott, 2009)(Wu et al., 2016). It is reported in hexagonal unit cell also where c-axis of the hexagon is parallel to diagonal of the perovskite with lattice parameters as $a=5.58 \text{ \AA}$ and $c=13.9 \text{ \AA}$ (Catalan and Scott, 2009). By applying suitable strain, changing the composition of the elements and by varying the temperature, the structure of BFO can be changed. Different crystal structures such as monoclinic, orthorhombic, tetragonal and triclinic are reported by applying suitable strain on the substrates and by doping (Durga Rao et al., 2014; M. H. Lee et al., 2015; J. B. Li et al., 2010; Muneeswaran et al., 2015; Yuan et al., 2007, 2006).

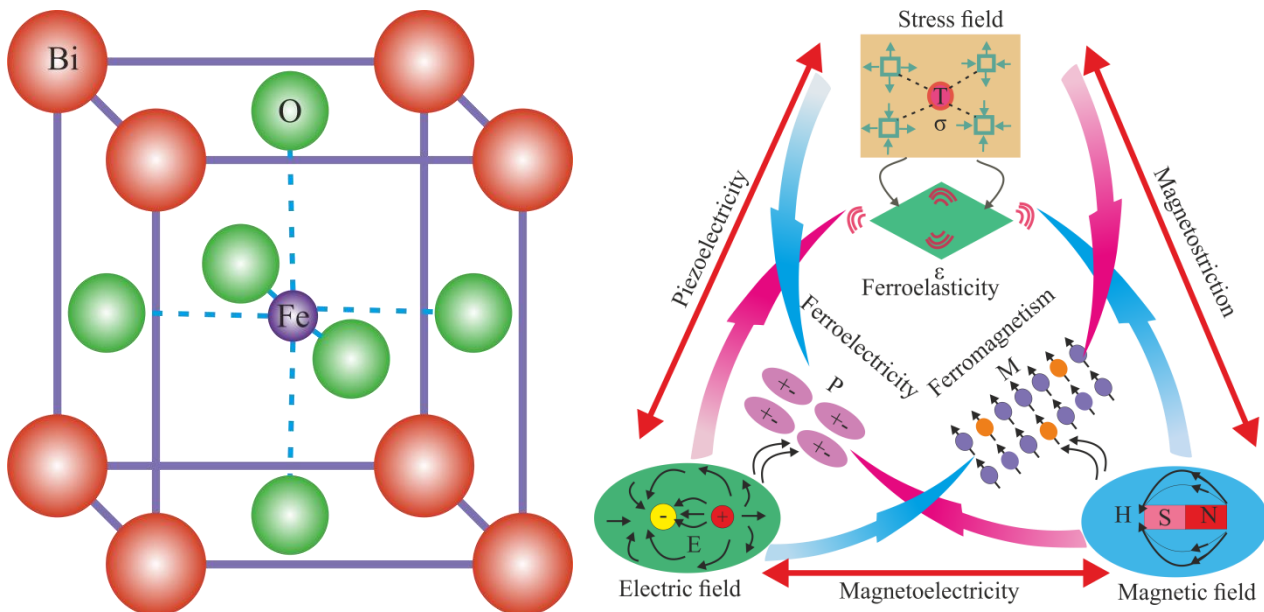


Figure 2.4 : Schematic of (a) Crystal structure and (b) Different ferroic properties existing in BFO.

2.2.2 Properties

2.2.2.1 Ferroelectric Properties

Ferroelectric properties of BFO are being studied since 1970s. It has Curie temperature $\sim 820^\circ\text{C}$. The first polarization was measured by Teague et al. in 1970 on bulk single crystal BFO and the measured spontaneous polarization was $3.5 \mu\text{C}/\text{cm}^2$ along $\langle 100 \rangle$ representing $6.1 \mu\text{C}/\text{cm}^2$ along $\langle 111 \rangle$ direction (Teague et al., 1970). They found that the expected value should be one magnitude higher than the obtained/measured value. They got unsaturated hysteresis loops and concluded that it is because of the high leakage current. This may be assigned to the imperfections in the bulk BFO material. After proving the ferroelectricity in BFO in 1970, very little research was done on this topic for next three decades. In 1999, Ueda et al. reported that the polarization is $2.5 \mu\text{C}/\text{cm}^2$ on a heterostructure 300 nm thin film of $\text{BiFeO}_3\text{-BaTiO}_3$ on an Nb doped SrTiO_3 substrate (Ueda et al., 1999). The mixture of another ABO_3 compound was taken into consideration to remove the secondary phase formation and to improve the resistivity.

In 2002, Palkar et al. reported $2.2 \mu\text{C}/\text{cm}^2$ polarization on PLD deposited BFO polycrystalline thin film on $\text{Pt}/\text{TiO}_2/\text{SiO}_2/\text{Si}$ substrate (Palkar et al., 2002). The breakthrough happened in 2003, when a large polarization $50\text{-}60 \mu\text{C}/\text{cm}^2$ was reported by Wang et al. on PLD deposited 200 nm thick epitaxial BFO thin film on $\text{SrRuO}_3\text{-SrTiO}_3$ substrate (Wang, 2003). They attributed this large polarization by explaining the change in lattice parameter due to epitaxial growth of the film on single crystal substrate. This breakthrough lured the scientific community to explore more about BFO in the following years. In the same year, Yun et al. reported the polarization of $35.5 \mu\text{C}/\text{cm}^2$ on polycrystalline BFO of thickness 350 nm deposited on $\text{Pt}/\text{TiO}_2/\text{SiO}_2/\text{Si}$ substrate by PLD (Yun et al., 2003). In 2004, Wang et al. fabricated highly resistive bulk BFO ceramic samples by liquid phase sintering technique and the estimated polarization is $3.5 \mu\text{C}/\text{cm}^2$ (Y. P. Wang et al., 2004). In 2004, Yun et al. demonstrated large polarization constant of $158 \mu\text{C}/\text{cm}^2$ on 300 nm thin BFO film deposited by PLD at 90 K temperature (Yun et al., 2004). In 2005, Neaton et al. estimated a polarization of $90\text{-}100 \mu\text{C}/\text{cm}^2$ on BFO using density function theory (DFT) which was consistent with reported experimental values (Neaton et al., 2005). The large polarization is attributed to ionic displacement of 6s lone pair of bismuth atom in BFO system. In 2006, Singh et al reported that 5 mole % Mn doped Mn:BFO based samples have large polarization of $100 \mu\text{C}/\text{cm}^2$ (S. K. Singh et al., 2006). It is suggested earlier that polarization of BFO depends on the crystal structure and physical properties which can be manipulated by applying different deposition techniques, temperature and doping. The super tetragonal

structure of BFO has become a focus of research community because it showed large polarization. In 2013, Yan et al. reported a high polarization of 230 $\mu\text{C}/\text{cm}^2$ on 10 mole % Ga substituted on Fe site in mixed tetragonal and rhombohedral structure of BFO (Yan et al., 2013). This was attributed to morphotropic phase boundary phenomenon. Fan et al. in 2015 showed large polarization of 150 $\mu\text{C}/\text{cm}^2$ in $\text{BiFe}_{0.6}\text{Ga}_{0.4}\text{O}_3$ film which showed a super tetragonal structure with a large c/a ratio >1.2 (Fan et al., 2015). In 2015, Guo et al studied polarization properties on tetragonal phase in BFO film (Guo et al., 2015).

2.2.2.2 Magnetic Properties

Bulk BFO exhibits G-type antiferromagnetism below Neel temperature $T_N=643$ K (Ramesh and Spaldin, 2007)(Catalan and Scott, 2009). G-type antiferromagnetic has both intra-plane and inter-plane coupling in antiferromagnetic order. For an ideal cubic perovskite type structure, each magnetic atom is surrounded by six AF neighbours in a G-type antiferromagnetic arrangement. Here, spin of one Fe ion is surrounded by six Fe ions antiparallel spins (Catalan and Scott, 2009). However, it has been reported that these spin are not entirely antiparallel which leads to existence of a weak canting moment. A super lattice is imposed on this canting with spin cycloid of antiferromagnetic sub-lattice with repeat distance of 62-64 nm (Lebeugle et al., 2008)(Sosnowska et al., 1982). Due to this, there is no net macroscopic magnetisation and electromagnetic coupling. It is reported that a strong magnetoelectric coupling and a net magnetization exists in some epitaxially grown BFO thin films which exhibits a net magnetization of 0.5 μ_B /unit cell (Wang, 2003).

It is shown that a weak ferromagnetism exist in BFO because of spin canting together with antiferromagnetism behaviour. It is caused by oriented magnetic moments perpendicular to the (111) plane. Dzyaloshinskii and Moriya (DM) interaction among the antisymmetric spin coupling is attributed to spin orbital coupling and exchange interaction (DZIALOSHINSKII, 1957)(Moriya, 1960). Later, this was supported by DFT calculations conducted by Spaldin et al.(Ederer and Spaldin, 2005). It has also been reported that at low temperature, a weak ferromagnetism occurs (Naganuma and Okamura, 2007)(Zhang et al., 2005). This ferromagnetism is attributed to presence of other impurity phases of BFO in small amount (Lebeugle et al., 2007). A weak magnetoelectric coupling exists in BFO, making it useful in multifunctional device applications by providing additional degrees of freedom to control magnetization or polarization (Spaldin et al., 2010)(Catalan and Scott, 2009). Here the control of magnetic dipoles by electric field and the control of electric dipoles by magnetic field have made BFO one of the most explored materials for data storage, sensors and actuators. The substitution of elements on A and B site of BFO has led to change in physical properties and in magnetoelectric coupling effects (Catalan and Scott, 2009)(Wu et al., 2016).

2.2.2.3 Other Properties

The estimated band gap of BFO is from 2.3-2.6 eV and is mostly reported as a direct band gap system (Clark and Robertson, 2007; Gujar et al., 2007; Ihlefeld et al., 2008; Palai et al., 2008). However, few reports have characterized it as indirect band gap semiconductor(Gujar et al., 2007). The computational results showed that the BFO is an indirect band gap with VBM at R point and CBM at Γ points (Palai et al., 2008)(Clark and Robertson, 2007). But the calculated flat valence band of rhombohedral crystal structure at room temperature makes it a direct semiconductor (Clark and Robertson, 2007). Type of band gap also changes when it changes its crystal structure from rhombohedral-orthorhombic-cubic (Catalan and Scott, 2009). The band gap is also a function of temperature and leads to metal-insulator (MI) transition (Palai et al., 2008). The MI transition is studied as a function of temperature and pressure (Palai et al., 2008). The reported pressure and temperature of BFO MI is 50 GPa and 1204 K, respectively at 1 atm pressure (Palai et al., 2008)(Gavriliuk et al., 2008). BFO is the single perovskite ferrite material

which exhibits MI transition (Catalan and Scott, 2009). The reported dc resistivity of the higher quality BFO is 10^{10} Ωcm and with the increase in temperature, this resistivity decreases (Palai et al., 2008). The radio frequency dielectric constant of BFO is 30 (Polomska et al., 1974)(Catalan and Scott, 2009). This value is obtained near to rhombohedral-orthorhombic transition because of the change from ferroelectric to paraelectric phase. The value of its refractive index is 2.62 leading to optical dielectric constant of 6.86 (Rivera and Schmid, 1997)(Catalan and Scott, 2009).

2.2.3 BFO Structures and Deposition Techniques

BFO can be synthesized by top down as well as bottom up approaches. The bottom up approach is preferable over top down approach because it has advantages of controlling the stoichiometry, doping, shape, pore size, functionalization, shape and surface area of the final product. BFO is reported in the form of bulk, thin film, nanoparticles, rods, wires and tubes by utilizing different deposition methods. Magnetoelectric (ME) effect is investigated widely for BFO based composites and laminates and in recent years the focus is shifted on nanostructures. ME effect in composite materials utilizes magnetic and ferroelectric properties of two different materials which are either separate but in close proximity or available in the core shell structure. Thin film materials have shown enhanced ME effect because of the mismatch between BFO and substrate, inducing strain during deposition.

2.2.3.1 Bulk BFO

BFO ceramic bulk is mainly prepared by solid state reactions. Solid state reaction uses oxide precursors as starting material. Solid state reaction is the first method which was used to synthesize BFO by mixing Bi_2O_3 and Fe_2O_3 oxides. These precursors were mixed and sintered at $700\text{-}800^\circ\text{C}$ for time duration of 30-120 minutes. However, later in 1967, it was reported that these BFO samples were not phase pure and contained certain impurities and also had low densities. It is shown that below 700°C , the BFO reaction is incomplete and between 700 and 750°C , few impurity phases are usually present. Further, above 750°C the BFO starts decomposing and becomes unstable (Wu et al., 2016). These impurities are present because of the evaporation of bismuth during sintering process. The presence of impurities in BFO causes large leakage current and poor polarization responses hence, synthesis of phase pure BFO is very necessary for any practical application. The present secondary phases are $\text{Bi}_2\text{Fe}_4\text{O}_9$, $\text{Bi}_{25}\text{FeO}_4$ and Bi_2O_3 . To avoid the formation of secondary phases, wet chemical methods, spark plasma sintering (SPS), and liquid phase sintering (LPS) are used (Wu et al., 2016). Liquid phase sintering utilizes the same technique as solid state reaction. Unlike solid state reaction, the prepared ceramic pellet is heated for short time duration at a given temperature. Wang et al. proposed a rapid LPS method to prepare high resistivity single phase ceramic BFO (Y. P. Wang et al., 2004). Further optimization is done to produce high quality BFO by Yuan et al. by having control over the particle size in the used material (Yuan et al., 2007). Decomposition of BFO at higher temperature leads to the formation of impurity phases which makes it difficult to synthesize high density BFO ceramic. SPS is another method which is used to overcome this problem. In this technique, densification of ceramics is done at lower temperature for a short span of time and high bulk density $\sim 96\%$ of theoretical value has been reported. Ferroelectric and magnetic properties of SPS synthesized BFO samples are relatively better in comparison to the conventional sintering. Dense lanthanum (La) and terbium (Tb) doped BFO ceramic samples are reported by Jiang et al. with enhanced ferroelectric and magnetic properties i.e. $P_r \sim 17 \mu\text{C}/\text{cm}^2$, $d_{33} \sim 12.8 \text{ pC}/\text{N}$ and $M_s \sim 0.71 \text{ emu}/\text{g}$ (Jiang et al., 2007). SPS suppresses loss of Bi and valence change of Fe ions which ultimately reduces the leakage current and improves electric and magnetic properties. Since, Bi ions controls the ferroelectric properties and Fe ions controls the magnetic properties hence, substituting suitable atoms at Bi and Fe sites can enhance these properties in BFO. Further, in BFO, leakage current can be suppressed by doping at Bi site by rare earth element. Doping by rare earth element also leads to the change in phase structure of BFO. The type and quantity of rare earth element affects the phase structure. The commonly

used rare earth elements are Sm, Nd, La, Tb, Pr, Gd, and Eu (Wu et al., 2016). Similar to Bi, Fe site can also be substituted which results in change in properties of BFO. However, substitution of atoms at Fe sites often results in poor ferroelectric and piezoelectric response but improved magnetic responses (Wu et al., 2016). The phase change in Fe substitution is almost negligible. The commonly used dopant atoms are Zn, Co, Mn, Ni and Nb. Substitution at both Bi and Fe sites are realized to improve both electric and magnetic properties of BFO. The doping at both the sites brings change in phase structure as well (Wu et al., 2016). Apart from that, the properties of bulk BFO are changed by making a solid solution of BFO by other perovskites compounds such as BaTiO₃ and PbTiO₃. Oxides additives such as MnO₂ and CuO are also added in BFO to improve resistivity and magnetic properties of BFO (Wu et al., 2016).

2.2.3.2 Thin Film

Thin film provides advantage over bulk due to defect free high quality film formation by controlling different parameters in several deposition techniques. The common growth techniques to deposit BFO thin films are PLD, MOCVD, RF sputtering, CVD, chemical solution deposition (CSD) and MBE (Safi and Shokrollahi, 2012). Wang et al. were the first ones to prepare epitaxial BFO thin film using PLD and demonstrated large polarization constant of 60 $\mu\text{C}/\text{cm}^2$ (Wang, 2003). The phase of BFO bulk is rhombohedral but in thin film the phase depends on substrate induced strain. The ferroelectric properties also depend on substrate thickness, orientation, type of the substrate and deposition technique (Wu et al., 2016). Ferroelectric response of BFO depends on orientation of the thin film. (111) oriented R3C BFO thin film deposited by RF sputtering methods showed large polarization ($2P_r=196.9 \mu\text{C}/\text{cm}^2$) and stable switching up to 5.25×10^7 cycles at 100 kHz frequency (Wu and Wang, 2009). Effect of low temperature polarization study is investigated by Yun et al. on polycrystalline BFO thin film deposited using PLD technique on Pt/TiO₂/SiO₂/Si substrate. Saturation polarization of 158 $\mu\text{C}/\text{cm}^2$ and remnant polarization of 146 $\mu\text{C}/\text{cm}^2$ are observed at 90 K temperature (Yun et al., 2004). Effect of buffer layer has been studied to minimize the leakage current in BFO deposited on Pt/Si substrate. The commonly employed buffer layers are SrRuO₃, BaPbO₃ and LaNiO₃. The BFO (111) oriented thin film is deposited by RF sputtering on SrRuO₃ buffer layer on Pt silicon substrate. The buffer layer enhanced (111) orientation of BFO film, reduced leakage current and observed polarization is 98.55 $\mu\text{C}/\text{cm}^2$. BiFeO₃ (101) oriented thin film deposited using PLD on SrRuO₃/SrTiO₃ substrate has shown $P_r \sim 80 \mu\text{C}/\text{cm}^2$. Same group have reported $P_r \sim 100 \mu\text{C}/\text{cm}^2$ for (111) oriented BFO and $P_r \sim 55 \mu\text{C}/\text{cm}^2$ for (001) oriented BFO film deposited by PLD techniques (Wu et al., 2016). BFO film on Pt/TiO₂/SiO₂/Si using PLD showed $P_r \sim 100 \mu\text{C}/\text{cm}^2$ (Wu et al., 2016).

MOCVD is another method which is used to realize BFO thin films. The source material used are in gaseous forms such as Bi((CH₃)₂(2-(CH₃)₂NCH₂C₆H₄)), Fe(C₂H₅C₅H₄)₂, and O₂. Another metalorganic gas source is Co(CH₃C₅H₄)₂ by using which dopants can be introduced easily (Saito et al., 2006)(Yasui et al., 2007). Pressure and temperature of the reactor is kept constant when using this precursor and mix gas pulses are applied for 10 sec and 5 sec respectively. Apart from gaseous precursors, liquid precursors are also used which are synthesized by mixing tris(2,2,6,6-tetramethyl-3,5-heptanedionate) bismuth(III) [Bi(thd)₃] and tris(2,2,6,6-tetramethyl-3,5-heptanedionate) iron(III) [Fe(thd)₃] in tetrahydrofuran (Zhang et al., 2016). A showerhead is used for liquid precursor delivery inside the system. Oil is used to heat the showerhead to prevent condensation during deposition of evaporated precursors hence, leading to large and homogeneous deposition of the film. It has been reported that Bi(mmp)₃ (mmp = 1-methoxy-2-methyl-2-propoxide) is a better liquid precursor than Bi(thd)₃, growth rate of which is comparable to Fe(thd)₃ precursor. To avoid the reaction between precursors prior to deposition, the evaporation temperature is kept below 300 °C and the substrate temperature is kept $\sim 550^\circ\text{C}$ which allows the highest growth for both Bi(thd)₃ and Fe(thd)₃ precursors (Zhang et al., 2016). The stoichiometry of Bi and Fe atoms are maintained by controlling the input gas flow for gaseous precursors. The molar ratio of Bi/Fe is linearly dependent on the ratio of gas

precursors used. $\text{Bi}((\text{CH}_3)_2(2-(\text{CH}_3)_2\text{NCH}_2\text{C}_6\text{H}_4))/\text{Fe}(\text{C}_2\text{H}_5\text{C}_5\text{H}_4)_2$ ratio of ~ 0.5 is required to obtain pure phase of BFO (Zhang et al., 2016). Hence, to have a control over ratio of precursors, the composition of film can be controlled. Similarly for liquid precursor also, the stoichiometry depends linearly on the Bi/Fe ratio. The amount of Bi precursor should be higher in comparison to iron precursor in the $\text{Fe}(\text{thd})_3$ and $\text{Bi}(\text{thd})_3$ precursors (Zhang et al., 2016). This is needed because vapour pressure of Fe precursor is 2.5 times larger than Bi precursors and also $\sim 70\%$ Bi precursors vaporises which leads to deficiency of Bi atoms (Zhang et al., 2016). Stoichiometry of the BFO film can also be maintained by utilizing heterometallic compound containing both Bi and Fe atoms (Zhang et al., 2016).

Chemical solution deposition (CSD) is one of the simplest techniques to deposit BFO thin film. Unlike PLD where both deposition and crystallization take place at the same time which results in high quality film, the deposition and crystallization takes place at different time in CSD. After gel formation, deposition takes place at lower temperature and crystallization at higher temperature. The critical steps in synthesizing thin film using CSD is to prepare defect free stable gel and then crystallization which does not results in any secondary phases. The gel preparation needs metal precursors, solvents and chelating agents. The precursors mixed in solvent result into a cross linked structure known as gel which is used for deposition later (Zhang et al., 2016). Metal alkoxides are used as precursors when the solvent is DI water. These precursors are costly and hence not economical for synthesis. Metal salts such as nitrates and chlorides are used for BFO deposition. Particularly metal nitrates $\text{Bi}(\text{NO}_3)_3 \cdot 5\text{H}_2\text{O}$ and $\text{Fe}(\text{NO}_3)_3 \cdot 9\text{H}_2\text{O}$ are investigated widely by the researchers due to its low decomposition temperature which reduces the carbon contamination in final product. Apart from that, these are highly soluble in water which is beneficial for hydrothermal synthesis as well (Zhang et al., 2016). Organic solvents such as 2-methoxyethanol (2-ME) and ethylene glycol (EG) are preferred over DI water because of its relatively better solubility for different compounds. It has linear structure which makes dense and homogeneous precursors molecules. These solvents also have higher viscosity and surface tension which makes it suitable to facilitate the growth of films in a particular direction, making the films oriented (Zhang et al., 2016).

Chelating agents such as tartaric acid, citric acid, and acetic acid affects the viscosity of the solution and reacts with precursors to make a stable gel (Zhang et al., 2016). The morphology of the final product depends on the molecular structure of the chelating agent hence, choosing a particular chelating agent is crucial for a required morphology of BFO (Zhang et al., 2016). The effect of heating on bonding of precursors has been studied by Zhang et al. they used acetic anhydride and metal nitrate in 2-ME and reported that the esterification of 2-ME and acetic acid is taking place which facilitates the formation of 2-ME acetate (Zhang et al., 2015). This esterification increases the drying time during spinning and heating and prevents from precipitation of precursors. The water molecule present in the metal precursor leads to precipitation of metal salts due to hydrolysis while heating. These precipitates are formed when samples dry before gelation and it leads to separate phase formation of bismuth and iron compounds resulting in impurities (Zhang et al., 2016). Bismuth has lower evaporation temperature than iron, crystallization temperature of CSD derived films are much higher than the melting point of Bi which results in high Bi losses. It introduces secondary phases of BFO as impurities hence; to avoid that, excess amount of Bi is considered during the gel formation. However, higher Bi content results in precipitation of metal salt and lower Bi content results in porous and inhomogeneous surface of the metal. Hence, an optimal window of metal precursors exists which facilitates in smooth and defect free film (Zhang et al., 2016). After optimization of the solution, the next step is deposition of thin film using a spin coater. The spin coating has several steps, firstly, the solution is poured on the substrate then the substrate is rotated at higher velocity which results in exclusion of excess solution. After that, the substrate is rotated with a constant velocity which results in a film formation and later the substrate is dried for

crystallization. The thickness of the films depends on several factors, and is directly proportional to viscosity and inversely proportional to density of the solution, spin velocity and spin time (Zhang et al., 2016). Thicker films obtained by high viscosity solution, low spin velocities, and smaller time often results in cracks hence it is advisable to repeat the deposition process of high spin velocity coated samples to get the thicker films (Zhang et al., 2016). Evaporation starts during spin coating due to increased air flow which results in precipitation of the metal salts. Hence, preheating the substrate up to gelation temperature before spin coating is a better way to obtain good quality film. After deposition, the film is subjected to the high temperature heat treatment to achieve high quality crystalline BFO thin film (Zhang et al., 2016). It is reported that BFO thin films are prone to secondary phases when annealed in oxygen atmosphere while pure phase BFO is synthesized when annealed in nitrogen environment (Zhang et al., 2016). Pure phase BFO thin film is also reported by incorporating high Bi precursor which has shown high polarization. The effect of oxygen pressure on BFO annealing has also been studied and reported that lower oxygen partial pressure results in loss of oxygen atom from Bi atoms by breaking Bi-O bond, causing Bi precipitation. This enhances the nucleation and results in polycrystalline thin film of BFO (Zhang et al., 2016).

2.2.3.3 Nanostructures

Several nanostructures of BFO such as nanoparticle, nanorods, wire and fibres have been synthesized by different deposition techniques. Nanoparticles are the 0 or 3 dimensional materials where particle size i.e. diameter may range from 1 nm to 100 nm. Sol gel method is a conventional route to prepare BFO nanoparticles. Doping can be done easily using this method by simply incorporating the dopant salts in appropriate stoichiometric ratio. Metal salts are mixed in 2-ME and the solution is heated at higher temperature (120-160 °C) to obtain powder form of xerogel (Chakrabarti et al., 2012)(Zhang et al., 2016). Another technique is by adding acid such as tartaric acid to form the solution and then the solution is heated to obtain the xerogel. These aqueous solution based methods do not use any organic solvent; instead it uses nitric acid together with acetic acid or tartaric acids, which acts as chelating agents (Zhang et al., 2016). Chelating agent plays a significant role in the final phase formation and morphology of particles. Decomposition of metal precursors leads to formation of nanoparticles. The dried particles are subjected to pyrolysis at ~400 °C to remove any organic impurities and then sintered at higher temperature 500-600 °C to get the final product. The size of nanoparticles depends on annealing temperature (Zhang et al., 2016). Hydrothermal method is another technique to prepare nanoparticles. Here, instead of organic solvent, water is used to dissolve the precursors. The crystallization of the particles takes place during the hydrothermal process and after that the product is washed, filtered, and dried to get the final product. Hydrothermal method uses minerals such as KOH, KNO₃ and NaOH along with metal salts dissolved in DI water (Zhang et al., 2016). Metal salts are put into dilute nitric acid which results in precipitates of Bi and Fe ions. These are then washed with DI and additional KOH is added in final product in the presence of dilute nitric acid (Zhang et al., 2016). Mineral free hydrothermal synthesis is also realized by using metal nitrates dissolved in DI and citric acid. Ammonia solution is then added in this solution to maintain the pH at about ~9. This solution is further kept in hydrothermal bomb and subjected to high temperature (150-220 °C) for 5-20 hours which results in higher pressure inside the bomb (Y. Wang et al., 2007)(Zhang et al., 2016). The product is then collected, washed, and dried to obtain the final product. The phase and structure of the BFO nanoparticles rely on the minerals added, and reaction conditions. Another method is microwave assisted hydrothermal process which have same precursors as hydrothermal with additional Na₂CO₃ and KOH as minerals. The solution is kept in hydrothermal bomb and is placed in microwave oven at temperature 160-230 °C for 30-60 minutes (Joshi et al., 2008). The resultant nanoparticles showed very small particle size ~10-50 nm. Another method to synthesize nanoparticles is auto combustion method where the metal precursors are added in DI water together with some fuels such as glycine (C₂H₅NO₂), sucrose (C₁₂H₂₂O₁₁), ethylene

glycol ($C_2H_6O_2$), ethanolamine (C_2H_7NO), citric acid ($C_6H_8O_7 \cdot H_2O$), urea (CON_2H_4), and stearic acid ($C_{18}H_{36}O_2$) (Yang et al., 2011). The resulting solution is further transferred into a teflon box, and heated to synthesize gel. The collected gel is then heated at ~ 300 °C in furnace to obtain BFO nanoparticles. Sol-gel method is used to obtain smaller particles at higher temperature whereas relatively larger particles are obtained by hydrothermal method at lower temperature (Zhang et al., 2016).

(a) Nanowires, Nanotubes and Nanofibers

1-D nanostructure should have diameter less than 100 nm and large ratio of length to diameter. Template based growth is preferred to synthesize BFO based nanowires and nanofibers (Zhang et al., 2016). Anodic aluminium oxide (AAO) membrane is generally used as a template for nanowire or rod growth. The precursors fill the pores of AAO template by capillary action and facilitate nanowires growth. The length and diameter of the nanowire depends on the diameter and thickness of the template, respectively. The heating temperature of BFO, grown using AAO, should be less than 800 °C as above this temperature BFO reacts with Al_2O_3 to form $Bi_2Fe_{4-x}Al_xO_9$ (Rørvik et al., 2011). The solution used for deposition can be either aqueous or non-aqueous as described earlier. Controlling pH of the solution is an important parameter as the high pH leads to precipitation of Bi and Fe ions due to presence of excess OH ions (Zhang et al., 2016). The substrate with AAO is placed in the precursor solution. After filling pores with precursors under capillary forces, nanowire growth takes place. When the precursors are deposited on the wall of the pores, formation of nanotubes facilitates. The size and morphology of nanotubes depend on the concentration of metal precursors and its viscosity, time of growth and thickness, and size of AAO pores. The deposited structure is then dried at 100-150 °C for 1-2 hours then subjected to pyrolysis at 400-450 °C followed by heat treatment at 650 °C for final BFO structure (Zhang et al., 2016). The AAO template is then removed by placing the substrate in 4-6 M NaOH solution for duration of 10-24 hours. Recently, template free growth of BFO nanowires has been demonstrated by Liu et al. using bismuth nitride and iron chloride as starting precursors (Liu et al., 2011). The precursors are mixed in acetone by stirring and ultra-sonicating and the pH is adjusted by water and concentrated ammonia up to 11-12. The final precipitate is washed by DI and centrifuged, further obtained product is placed in NaOH and hydrothermal synthesis is done at 180 °C for 72 hours. The dried powder had diameter ~ 45 -200 nm and length ranging from few hundred nanometres to microns.

Nanofibers also have the same precursor materials which are used for synthesis of BFO by spin coating process. The precursor solution of 2-ME is further subjected to 1:2 of acetone and N,N-dimethyl formamide (DMF) along with poly(vinyl pyrrolidone) (PVP) to adjust the viscosity of the precursor solution. Instead of 2-ME, 1:2 of water and acetone mixture is also used as a solvent followed by adding PVP and nitric acid in ethanol. Finally a chelating agent 2,4-pentanedione is added to obtain the final solution (Zhang et al., 2016). Electrospinning method is generally used to deposit nanofibers. In this method, solution is filled in syringe having stainless steel needle and the needle is connected to positive bias, aluminium is used as a collector and is grounded. The distance between syringe and collector is kept around 10-13 cm. The feed rate is controlled by syringe pump and the rate is maintained 0.5-0.9 ml/hr. the needle produces charge droplet which is stretched because of charge repulsion and surface tension which forms fibre shaped jet towards the collector. The substrates are placed on the collector to collect nanofibers (Fei et al., 2015).

2.2.4 Devices

Ferroelectric and piezoelectric characteristics of BFO have been used for different applications. BFO has large remnant polarization ~ 100 $\mu C/cm^2$ along [111] polar direction. This

is the highest switchable polarization in any lead free material and hence, it makes a good candidate in ferroelectric memories in comparison to its most widely used counterpart PZT (Catalan and Scott, 2009). Unlike PZT, BFO doesn't have any lead content hence it is health and environment friendly. This is one of the reasons that BFO is being considered as a substitute to PZT based ferroelectric memories. However, BFO suffers from dielectric loss, thermal decomposition near to coercive voltage and fatigues. These barriers need to be eradicated in order to use BFO as next generation ferroelectric memory devices. Few approaches are developed to resolve these problems, which are ion substitution, oxide buffer layer incorporation, making of solid solutions with other ABO_3 perovskites and heterostructure formation. Polarization constant of 130-230 $\mu\text{C}/\text{cm}^2$ is reported in Ga-BFO which is attributed to the change in phase structure (Wu et al., 2016). Piezoelectricity is another property of BFO which makes it useful for several potential applications. Temperature dependent piezoelectric properties are important for high temperature piezoelectric device applications. BFO has high Curie temperature $\sim 830^\circ\text{C}$ which is suitable for high temperature requirement however, the piezoelectric coefficient of BFO is low and hence it opens up another field of research to improve this property. Several approaches are used to improve piezoelectric properties which are ion substitution, secondary phase addition, deposition technique optimization, and strain modification (Wu et al., 2016). Ion substitution by many rare earth elements has shown improved piezoelectric response in BFO. Large piezoelectric coefficient is observed in Tb or Sm doped BFO and the reported value is $\sim 95\text{-}140\text{ pm}/\text{V}$ (Wu et al., 2016).

Formation of morphotropic phase boundary (MPB) is another technique to improve the piezoelectric coefficient of BFO. Rhombohedral phase of BFO combined with tetragonal phase of PbTiO_3 leads to MPB when the concentration of PbTiO_3 is 30 mole % (Wu et al., 2016). This MPB is believed to be the reason for high piezoelectric coefficient of PZT. Solid solution of BFO and orthorhombic SmFeO_3 has been reported to have large piezoelectric coefficient. Another important aspect of BFO is its magnetic properties. A weak magnetization exists in BFO at room temperature. Magnetic properties of BFO are enhanced by several techniques such as by synthesizing different morphologies, mixing with another magnetic compound and chemical modifications. Elemental doping is investigated widely in BFO to enhance its magnetic properties. The physical mechanism to understand the enhanced magnetic properties has been studied and the reasons are attributed to the presence of fractional Fe^{2+} , change in phase structure, spatial homogeneous arrangement of spin, variation in Fe-O-Fe canting angle, and spin cycloid structure distortion (Wu et al., 2016). Substitution of Tb on Fe site has shown improved magnetic property which is assigned to spin interaction between Fe^{3+} and Tb^{3+} , and also bond interaction between Tb-O and Bi-O (Wu et al., 2016). BFO deposited on Pt/Ti/ SiO_2 /Si showed strong saturation magnetisation whereas film deposited on LiNbO_3 showed small response. The reason is attributed to substrate induced strain in BFO thin films (Wu et al., 2016). ME coupling is another property which is exploited for several applications such as magnetic energy harvester, low power read head for hard discs, and magnetic field sensors. However, the ME coupling coefficient of BFO at room temperature is low and investigations are carried out to improve that property. Destroying long range spin cycloid and bringing the transition temperature to RT are another interesting approach, used by Kimura et al. to improve the coupling coefficient (Wu et al., 2016). Apart from that, processes such as solid solution and ions substitution are explored to increase the ME coupling of BFO. Another application of BFO is terahertz radiation generator which has been demonstrated by Takahashi et al. (Takahashi et al., 2006). When a femtosecond pulse hits the thin BFO film then THz radiation is generated which can be used in telecommunications and security applications.

2.2.4.1 Spintronic

The most important application of BFO is in spintronic. The ME coupling in BFO at room temperature allows changing the polarization by magnetic field and magnetization by electric

field. This property allows fabricating an energy efficient spintronic device in which information is stored by magnetic means and it is written electrically. The voltage writing is beneficial because it can be used in an electronic circuit without any mobile parts, energy requirement is low. Further, the voltage is thickness dependent, which automatically scales (Catalan and Scott, 2009)(Sando et al., 2014). The reading process by magnetic means has advantage that it is non-destructive and does not involve any kind of switching phenomenon. Since these memories work on magnetic states hence, these states should be switchable by using electric field as well readable by magnetic field. Spins in BFO is coupled with crystal lattice and due to that, rotation in polarization results in rotation in magnetization sub-lattice. This means that the antiferromagnetic state can be changed by a bias voltage application enabling the switching of magnetic state by electric field. However, reading magnetic states by antiferromagnetic switching is not possible as these states are not generally readable. Exchange bias is a technique which is used to read antiferromagnetic states (Catalan and Scott, 2009)(Sando et al., 2014). This is a phenomenon where spin interaction prevails between top of antiferromagnet and a thin ferromagnet (FM) attached with it. This exchange bias results in the widening or offsetting in hysteresis loop of ferromagnetic layer. The voltage induced magnetic changes in antiferromagnetic layer changes the hysteresis of ferromagnetic layer which then becomes readable by conventional method. BFO based system with strip like domain morphology; exchange bias results in enhanced coercive field whereas with mosaic like domain in BFO, exchange bias results in widening of hysteresis loop. Malozemoff's exchange bias model predicted that exchange bias in BFO/FM system is due to spin interaction between antiferromagnetic domain walls of BFO and FM domain walls. Electrical manipulation of exchange bias is possible in ME coupled BFO which further allows the manipulation of FM thin layer by electric means (Sando et al., 2014). This is reported on $\text{Co}_{90}\text{Fe}_{10}$ dots on BFO layer as investigated using synchrotron, PFM, and magnetotransport studies. The magnetotransport studies showed that by applying a large voltage, the polarization of BFO can be rotated by 71° and thus resulted in 180° reversible change in net magnetization of $\text{Co}_{90}\text{Fe}_{10}$ dots which is substantiated by shift in angular dependence of magnetoresistance in $\text{Co}_{90}\text{Fe}_{10}$ (Heron et al., 2011). Vertical configurations of devices are preferred from integrated electronics point of view enabling it to operate at lower temperature. Allibe et al. analysed electrical control of magnetic states of BFO spin valve exchange bias. Reduction in strong bias is observed by applying moderate voltage on $\text{Co}_{72}\text{Fe}_8\text{B}_{20}/\text{Cu}/\text{Co}$ spin valve which is evident in giant magnetoresistance (GMR) shift (Allibe et al., 2009). Additionally, BFO is used as barrier layer in spintronic applications. Tunnelling magnetoresistance is observed in BFO sandwiched between two FM metals, where BFO is insulating up to the tunnelling thickness. BFO is switchable ferroelectric up to 2nm thickness which makes it a suitable candidate for switchable tunnel junction and the polarization rotation control of magnetic states of FM electrodes leads to modified tunnelling MR (Béa et al., 2006). Gajek et al. showed that both magnetic and electric field can be used to control the tunnelling resistivity and thus, giving rise to four state memory devices (Gajek et al., 2007). The accumulation as well as depletion of charges on BFO based FeFET based devices changes the magnetic properties of nearby manganite channel. Cooling of BFO/LSMO system in the presence of magnetic field induces an exchange bias which further induces magnetic moment in BFO. Magnetic coercive and exchange fields are dependent on polarization direction which is inferred from its magnetoresistance studies. This exchange bias controlled by electric field is reversible, provided temperature is below 30 K (Wu et al., 2013)(Calderón et al., 2011).

2.2.4.2 Optical Devices

BFO has its applications in optical devices because of its large birefringence. The optical axis depends on the direction of ferroelectric polarization. Hence, change in refractive index (~ 0.2) is possible by rotating the polarization direction of BFO. This effect is used to develop a plasmonic resonator or switch by using a gold wire grating on 500 nm thin BFO film. The device showed modulated reflected beam (30 dB) which depends on the polarization of BFO (Sando et

al., 2014). BFO also has size dependent opto-electronic properties and hence, it can be used as optical modulators. However, certain problems need to be addressed such as how to synthesize single domain thick BFO film, and how to guide the laser along the modulator length for long duration so that it can produce modulation without high losses. It is suggested that deposition of BFO on low dielectric constant substrate yields wide bandwidth and frequency modulation. Tetragonal phase of BFO has higher ferroelectric distortion than rhombohedral phase and hence, shows more birefringence (Sando et al., 2014). Photostriction effect is also observed in bulk BFO, which is likely to arise from combination of photovoltaic and inverse piezoelectricity. This effect is magnetic field dependent which is evident by spin-lattice coupling (Sando et al., 2014).

2.2.4.3 Electronic Devices

Ferroelectric field effect transistors (FeFET) utilize the large polarization of BFO and the devices are used in planar configurations usually. The devices using vertical configuration is known as ferroelectric diodes/tunnel junctions. In case of FeFET, the current flows from a channel near to ferroelectric and in diodes, the current flows across the ferroelectric using different transport mechanism in different regimes (Sando et al., 2014). BFO is an attractive material as gate oxide for FeFET. R and T phase of BFO makes it interesting materials which can accommodate a large lattice mismatch of different materials. Smaller lattice constant of Ce doped CaMnO_3 has made it a compatible channel material with T-type BFO gate dielectric for FeFET applications. The observed ON/OFF ratio is 10 at 200 K however, no changes in the ratio is observed when the thickness of the channel reached below 20 unit cell. The reported sheet carrier density modulation is $0.6 \times 10^{14} \text{ cm}^{-2}$ with corresponding polarization $\sim 11 \mu\text{C}/\text{cm}^2$. This reported value is an order of magnitude less than the expected value of T- BFO (Yamada et al., 2013). LMSO and R-BFO combination is also tried for FeFET applications and at lower temperature change in resistance is observed by a factor of 3 (Wu et al., 2013). A combination of R-BFO and superconducting ultrathin $\text{YBa}_2\text{Cu}_3\text{O}_{7-\delta}$ (YBCO) has also been investigated and the reported carrier concentration is $1.8 \times 10^{14} \text{ cm}^{-2}$, polarization $30 \mu\text{C}/\text{cm}^2$, and the critical super conducting temperature is 30 K (Ahn, 1999).

Polarization dependent diode characteristics are also reported in BFO. Ag/BFO/Ag diode showed asymmetrical I-V curve and when polarization direction is changes, the diode characteristics reversed. It is observed that the device's resistance strongly depends on the direction of polarization in BFO based diodes. Very thin BFO based capacitor has quantum tunnelling mechanism for charge carriers which dominates the transport mechanism at lower bias voltage and its smaller thickness. Barrier height plays an important role in tunnel transmission and this height depends on the polarization type which produced resistance switching (Sando et al., 2014). BFO also produces giant electro resistance and has been reported by a few groups. Hambe et al. reported electroresistance of 80% in 3 nm thin R-phase BFO. Photovoltaic effect has also been reported in BFO because of it relatively smaller band gap and robust polarization together with better DC conductivity. Smaller band gap $\sim 1.5 \text{ eV}$ is reported in $\text{Bi}_2\text{FeCrO}_6$ (BFCO) by modifying the Cr/Fe ratio and the efficiency reported is 8.1 % in this double perovskite structure (Nechache et al., 2015). BFO based heterojunction is also investigated for photovoltaic effect. BFO/ZnO nanorods/PEDOT:PSS based heterojunction showed conversion efficiency of 0.17%. The front and back contacts are FTO and Au and the Schottky barrier of FTO/BFO along with smaller resistance of ZnO/PEDOT:PSS and high carrier transport of nanorods played a significant role in achieving such efficiency (Wu et al., 2014). $\text{In}_2\text{O}_3\text{-SnO}_2/\text{ZnO}/\text{BiFeO}_3/\text{Pt}$ based heterojunction showed conversion efficiency $\sim 0.33 \%$ under a blue monochromatic light illumination (Fan et al., 2014). Thin BFO film with striped domain has shown an interesting PV effect which has resulted in higher voltage than the band gap. Ferroelectric domain wall concept was proposed to understand this behaviour of BFO (Lu et al., 2015). According to this model, the polarization induces built in potential in domain walls,

which is capable of separating photogenerated electrons and holes. This separation of electron and holes causes an accumulation of charge particles on the domain wall which further results in formation of electric voltage across the sample. There are several mechanism proposed to support the PV effect in BFO such as bulk PV effect, domain wall theory and Schottky barrier (Wu et al., 2016). Ferroelectric resistive switching is another aspect which has been observed in BFO based capacitor structures. High and low conductance states of BFO under polarization reversal is able to store binary information (Wu et al., 2016). BFO based tunnel junctions or diodes have shown high ON/OFF ratio $\sim 10^5$. This effect is attributed to the high polarization of BFO and the reported endurance is up to 10^7 cycles (Jin Hu et al., 2016). The switching speed is in microseconds and is not enough as the speed in ferroelectric switching could reach up to nanoseconds. There is still no consensus over the mechanism governing the switching phenomenon.

2.2.4.4 RRAM

Resistive random access memories store binary information by changing its resistance from low to high and vice versa. It has gained tremendous attention from the research community because of its excellent scalability, simple structure, compatibility with IC, large storage capacity, low power, high endurance, and more interestingly the non-volatility. Properties of different non-volatile memory devices are tabulated in table 2.4. RRAM devices are simple MIM structure where the sandwiched layer is either a semiconductor or high K dielectric material and the top and bottom contacts are either inert or active metals. Applied voltage on the device changes the resistance from high resistance state (HRS) to low resistance state (LRS). These HRS and LRS states are able to store binary data 1 and 0, respectively. The change in resistance from HRS to LRS is termed as set state and from LRS to HRS is implied as reset state. In some oxide material, another process, which is known as forming, is needed. Forming allows a soft breakdown of oxide materials which are initially in insulating state and generally a high voltage is required to facilitate the forming. This step is not desirable as it leads to large power consumptions (Chang et al., 2016). RRAM is categorized in two types unipolar and bipolar, depending on applied voltage polarity to change the states from set to reset and vice versa. Schematic of these devices are shown in figure 2.5 (a & b). In unipolar devices, same polarity of voltage but with different magnitude is used to change set to reset states and vice versa. Thermal effects such as joules heating hold an important role in changing the set and reset states. The writing voltage is high in comparison to erasing voltage in unipolar devices. In bipolar, one type of polarity of applied voltage is used to change the HRS to LRS and other type from LRS to HRS. Another type of RRAM is non polar RRAM in which switching of set to reset and vice versa is induced by either positive or negative voltage. Usually compliance current (CC) is applied on the devices to prevent them from permanent breakdown of the device (Wong et al., 2012).

Table 2.4: Different Memory Technology and Properties (<http://www.itrs.net/>)

Feature	SRAM	DRAM	NAND flash	STT-MRAM	FeRAM	PCM	RRAM
Feature size (nm)	45	36	16	65	180	45	<5
Cell size (F ²)	140	6	4	20	22	4	<4
Read time (ns)	0.2	2	25000	35	40	20~70	<10
Write time (ns)	0.1~0.3	10~50	100000	13~95	65	50~500	20~30
Retention	as long as voltage applied	<sec.	~10 yr	>10 yr	>10 yr	>10 yr	>10 yr
Endurance (cycles)	10^{16}	$>10^{17}$	10^5	10^{12}	10^{14}	10^9	$>10^{12}$

Energy per bit (pJ)	0.0005	0.004	101~104	0.1~1	6	2~100	0.0001
---------------------	--------	-------	---------	-------	---	-------	--------

Many mechanisms are reported to understand the switching phenomenon in RRAM devices. These are classified in two types: filament model and the interface models. The filament model depicts that HRS is changed to LRS by forming a conducting filament (CF) between top (TE) and bottom electrode (BE). This filament can be either due to movement of anion or cation. In anion migration, oxygen vacancies present in oxide material and the model is termed as valence change memory (VCM). In cation migration, the filament is formed by movement of the metal cation from one electrode to another. This is known as conducting bridge RAM (CBRAM) (Chang et al., 2016). The metal electrode should be active metal such as silver (Ag) and copper (Cu) which on application of bias should be able to migrate inside the material. Moreover, inert metals such as Pt and Au lead to VCM type of mechanism. Type of electrodes also plays important role in type of switching as well as polarity dependence HRS and LRS states. Metal ions migrate inside the material after applying bias voltage, which leads to formation of conducting filament, bringing HRS to LRS. By changing the polarity of applied voltage, the filament is dissolved leading LRS to HRS. The disrupter in filament is explained by two methods.

For VCM, the application of voltage facilitates large flow of current which generates Joules heating effect, further leading to rupture of filament. This is known as thermochemical effect (Chen et al., 2017). For CBRAM, the applied voltage leads to rupturing of the filament and is known as electrochemical reaction. The device characteristics are independent of the cell area and the thickness of the electrode. In interface model, the switching is facilitated by changing the barrier height of the insulator/metal junction. This barrier height can be modulated by applied electric field which results in changed transport properties. Models such as ion migration assisted filament formation, charge trapping de-trapping and polarization induced switching have been reported. The ion migration in interface type switching is different from filamentary switching as in former, only interface plays the role. Charge trapping/de-trapping mechanism explains that the charge is trapped at the interface which affects Schottky barrier height and further changes the resistance states of material (Chen et al., 2017). There are several performance parameters of RRAM which needs to be addressed in order to have a reliable device. The parameters are operating voltage, operating speed, endurance, retention, on/off ratio, reliability, multilevel storage, and device yield. The operating voltage of RRAM should be as low as possible. This is because high operating voltage requires high power consumption which is not desirable. It also affects the reliability of the devices. The already commercialised flash memory also suffers from high operating voltage; hence in order for commercialization of RRAM, it should work at low voltage (few mV) (Li et al., 2011). Operating speed is defined as time taken by the device to read and write. The operating speed up to nanoseconds is reported however, the much smaller value of operating speed will make the device more efficient.

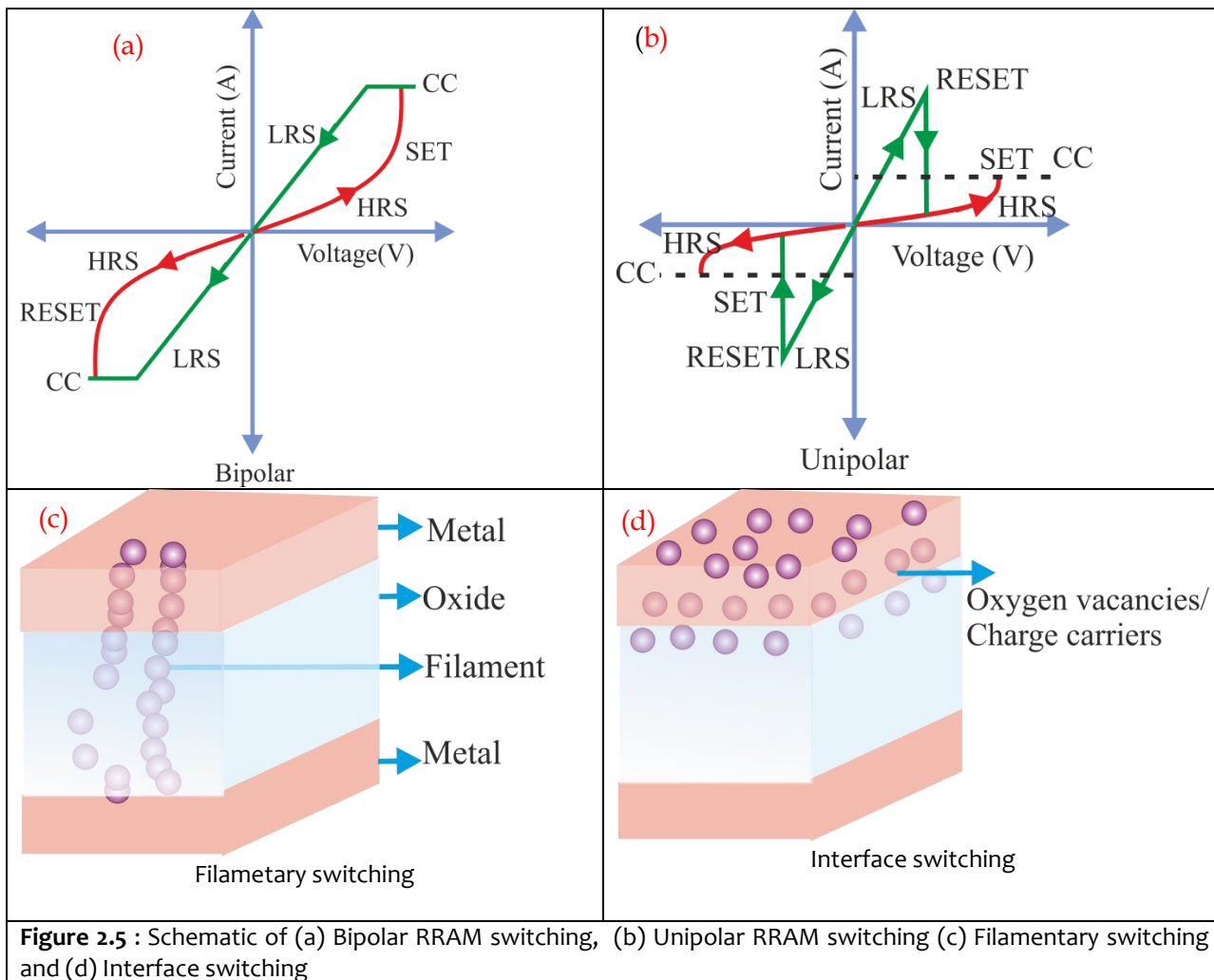


Figure 2.5 : Schematic of (a) Bipolar RRAM switching, (b) Unipolar RRAM switching (c) Filamentary switching and (d) Interface switching

Best reported operating speed for RRAM is between 5-100 ns (Li et al., 2011). The device needs to be switched between LRS and HRS and this term is known as endurance. Endurance can lead to the degradation of the device. Thus, it should be able to endure maximum number of set /reset cycles before leading to non-distinguishable LRS and HRS states. The reported value of endurance for flash memory is between 10^3 - 10^7 and the RRAM memory devices needs to show endurance for same or more number of cycles. Retention time is explained as the time duration over which the device will maintain its resistance after programming. The higher the retention time, better is the device. The device should be capable of retaining its resistance state for at least 10 years (Li et al., 2011). ON/OFF ratio is the ratio of resistances in ON and OFF state and the minimum value required is 10 i.e. one order to distinguish HRS and LRS. Much higher values up to six or seven order of magnitude have been reported for RRAMs, high value of the ratio substantiates a high density device with multilevel storage capability. Reliability is another aspect which tells that how the device is maintaining its set and reset voltage in multiple operations. Multilevel storage is desirable in memory devices to storing multiple bits in different resistance states. Large resistance ratio is required to distinguish between the stored multiple bits in the device. No control over the presence of oxygen inside the material leads to poor device yields and need to be addressed. Various techniques such as electrode material selection, doping and introduction of metal nanocrystals have been used to improve the device yields of oxide based RRAMs (Li et al., 2011). BFO based RRAM is explored in recent few years to understand its potential as commercial non-volatile memory.

2.2.5 BFO Based RRAM

Both unipolar and bipolar RRAM has been reported on BFO. Shuai et al. has reported a bipolar resistive switching in Au/BFO/Pt sandwiched structure where, BFO was deposited by PLD (Shuai et al., 2011). The device showed forming free behaviour and the reported resistance ratio is of two orders of magnitude. The switching mechanism is assigned to interface modulating charge trapping-de-trapping which is induced by applied electric field. Same authors again investigated a bipolar resistive switching in Au/BFO/Pt/SiO₂/Si configuration and proposed the electron trapping effect is the responsible mechanism for these devices (Shuai et al., 2012). Lin et al. has shown forming free bipolar resistive switching on PLD deposited Au/BiFeO₃/SRO heterostructure (Lin et al., 2014). The reported resistance ratio is 30 and retention was measured up to 10⁴ s. The endurance was measured upto 200 cycles. Oxygen vacancies migration or charge trapping/de-trapping model is attributed for such bipolar behaviour of the devices. Chen et al. has presented bipolar resistive switching in CSD deposited Pt/BiFeO₃/LaNi_{0.95}Fe_{0.05}O₃/Si structure (Chen et al., 2014). The device showed resistance ratio of 20 with retention time upto 10³ s and switching mechanism is attributed to oxygen vacancies migration model. Gao et al. investigated bipolar resistive switching in hydrothermally grown epitaxial BFO on Pt/BFO/NSTO heterostructure configuration (Gao et al., 2015). No degradation in resistance window is observed for 1500 s and the endurance was monitored for 200 cycles. Carrier trapping/de-trapping is attributed to be responsible for bipolar resistive switching in this device. They also showed that resistance states of the reset states can be changed by applying different reset voltages, substantiating multilevel storage capabilities of the device. Katiyar et al. reported unipolar resistive switching in sputtering deposited Pt/BFO/Pt device configuration (Katiyar et al., 2015a). The device showed resistance ratio of 10⁴ and the retention time was maintained for 3000 s. Chen et al. investigated unipolar resistive switching in CSD deposited Pt/BFO/Pt/Ti/SiO₂/Si devices (Chen and Wu, 2010). The resistance ratio of 10³ is observed for these devices and the switching mechanism is attributed to carrier injection and emission due to oxygen vacancies.

2.3 Characterization Techniques

The device application of the material requires understanding of different properties such as crystal structure, surface morphology and topography, elemental composition, defects, optical and electrical properties. There are several techniques to investigate these information. This section is a summary of several characterization methods used to identify and understand the phase, morphology, optical and electronic properties of different samples used in this thesis.

2.3.1 X-Ray Diffraction (XRD)

Periodically arranged atoms of a crystal lattice interact elastically with short wavelength rays and produces diffraction patterns following Bragg's angle of diffraction. The angle of diffraction depends on the materials' crystal structure. The criteria to obtain diffraction peaks are that the incident wavelength should be nearly equal to the interatomic spacing in the crystal. X-rays have short wavelength and thus, fulfils the criteria of diffraction. German scientist Wilhelm Conrad Rontgen first discovered X-ray in 1885. X-ray have wavelength in the range of 0.01-10 nm and the energies vary between 100 eV-100 keV.



Figure 2.6: Optical image of XRD system, IIT Jodhpur

XRD is a non-destructive powerful method to analyse crystal phase structure, lattice parameters, preferred orientations of phases, crystal symmetry, strain in lattice, and qualitative/quantitative phase composition of crystalline and polycrystalline materials. X-ray diffraction system comprises of major components which are X-ray generator, diffractometer assembly, and collection system together analysis tools. The X-ray generator generates X-ray by bombarding targets such as copper or molybdenum with high energy electron, inside a vacuum tube. The high energy electrons knocks out the electron from ground state of the target atoms which produces characteristics X-rays after refilling of those energy states by electrons from the next states. These X-rays are made collimated by passing through a Soller slit and collimated X-rays are again passed through a divergence slit to fall on the sample which is kept in a sample holder. The diffracted X-rays are collected at the detector and the analysis is done using software which has database for all the probable materials. X-ray diffraction studies of our all samples are done by using Bruker's D8 Advance Powder X-ray diffractometer (figure 2.6) which has a characteristic Cu- α wavelength of 1.54 Å as source of X-ray radiation. The parameters of the X-ray diffraction for different samples are described in the respective chapters.

2.3.2 Scanning Electron Microscope (SEM)

Scanning electron microscopy is a technique, used to analyse the topography of materials varying from nano to micro size range owing to its high resolution. It uses a focused electron beam for scanning the sample under vacuum conditions. It offers advantages over optical microscopy such as much larger magnifications because of smaller wavelength of electron in comparison to optical wavelengths and higher depth of field. The electron beam is thermionically emitted by tungsten filament and is then focused by a series of electromagnetic lenses which results in high resolution scanning source with a spot size of 4-5 nm. Two types of electrons are emitted when the beam strikes the samples. Low energy secondary electron is used for imaging and determines the topography of the specimen. High energy backscattered electrons which are used for contrast imaging, is helpful in determining the defects. It also provides information on the phase separation of multiphase specimen. Emitted secondary electrons are limited to upper part of the surface and hence are used in imaging whereas the backscattered electrons go inside the samples and hence used for phase separation analysis. Different detectors are used to detect secondary and back scattered electrons. X-ray is also generated in this process which is further used to find materials' elemental composition. We have used Carl Zeiss SEM EVO 18 system (figure 2.7) for surface topographic information and cross-sectional information of the prepared samples, details of which are explained in the subsequent chapters.



Figure 2.7: Optical image of (a) SEM and (b) DC sputter coating system , IIT Jodhpur

2.3.3 Energy Dispersive X-ray Spectroscopy (EDS)

When electron strikes the sample, various wavelengths are released by the samples. X-rays are emitted when the high energy scanning electrons knock out the electrons from inner orbit of the atoms and the electrons from outer orbits fills the electrons. The produced X-rays are characteristics of particular orbit from which it is originated and the material. This X-ray is separated from other signals and the counted X-rays are plotted with respect to energy to obtain the EDS spectra. This spectrum is used in determining the atomic and weight percentage of elements of the materials. IIT Jodhpur has Oxford make (X-act) EDS detector which is enclosed with Carl Zeiss SEM EVO 18 system which is used for analysis of different samples as a part of this thesis.

2.3.4 Atomic Force Microscopy (AFM)

Atomic force microscopy (AFM) gives 3D information about the surface roughness, depth, and topology of the samples. It was first presented in 1986 to analyse the surface properties of insulating materials(Maver et al., 2016). AFM contains a cantilever usually made of silicon carbide along with an attached sharp tip. The tip is transported closer to the sample and the force between tip and material is measured. The force is calculated by Hook's law and uses distance between sample-tip and spring constant of the cantilever to measure the force. The deflection in the tip is computed by measuring the variation in laser beam and the deflected beam using a photodiode. This variation is used to map the height of the sample which is further used to measure surface root mean squared (RMS) roughness. RMS represents average variation in samples' height over the scanned area. Average grain diameter can also be estimated from the planer view projection of the sample. Presence of micro level defects such as pits and foreign particles can also be observed from this technique. This is used in contact/ non-contact mode. The contact mode allows touching of the tip into layer which may damage to the surface sometimes because of the presence of water droplets or other foreign molecule on the sample. The non-contact mode uses van Der Waal (vdW) forces of attraction between tip and the surface. This technique often suffers from weak resolution because of weak nature of vdW forces. We have used Park scanning probe microscopy (SPM), XE-70 system (fig 2.8) to investigate the morphology, surface roughness, existing surface defects, and to calculate samples grain size, wherever required.

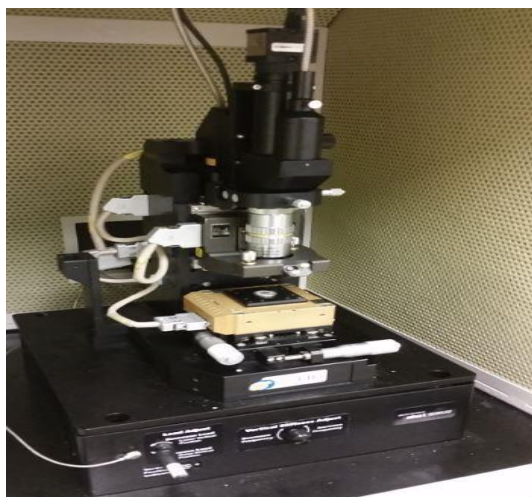


Figure 2.8: Optical image of AFM system, IIT Jodhpur

2.3.5 UV-Vis Spectroscopy

Ultra violet-visible (UV-Vis) spectroscopy refers to absorption, transmission or reflectance spectra in ultra violet and visible range. Light is produced by source/sources, which is further passed through a monochromator to generate the desired wavelength of light. The sample is subjected between monochromator source and detector. Transmission spectra provide the percentage of transmitted light passing through the sample. Light is absorbed by the sample when the energy of the light wave is greater than or equal materials' band gap. It is possible to calculate the thickness as well as the band gap of the sample by using these spectra. Tauc plot is a popular method to determine the band gap of the material. It is a graph between $(\alpha h\nu)^n$ and energy where, $n=2$ when the material has a direct band gap and $\frac{1}{2}$ when the material's band gap is indirect. Here, h is the Planck's constant and ν is the frequency of the incident photon. The linear region of the Tauc plot touching X-axis gives the value of band gap.

We have used Carry 4000 UV-Vis spectrometer supplied by Agilent technologies (figure 2.9) to measure optical properties of our samples. Substrate and material coated substrates are taken as reference and sample, respectively, for reflectance and absorption measurements. Diffuse reflectance spectroscopy (DRS) is done with the accessories attached with the system. This system allows the collection of diffused and specular reflectance. A polytetrafluoroethylene (PTFE) sample is used as reference for DRS measurement. PTFE is white and has reflectance above 99% in wavelength range of 300-1800 nm.



Figure 2.9: Optical image of Cary 4000 UV- Vis spectrophotometer

2.3.6 Raman Spectroscopy

Raman spectroscopy utilizes Raman Effect which was first reported by Raman in 1928(Singh, 2002). Here, a monochromatic photon source of visible, near infrared or near ultraviolet wavelength is allowed to interact with the specimen. Both elastic and inelastic scattering takes place after light-sample interaction. The major portion of scattered light is elastic and has the equal wavelength to the incident light, and is known as Rayleigh scattering. The inelastic scatterings are of two types: Stokes and anti-Stokes scattering. When the scattered frequency is lower than the incident frequency then it is termed as Stokes scattering. If the scattered frequency is higher than the incident frequency then it is identified as anti-Stokes scattering. The anti-Stokes scattering has weaker intensity as it requires the molecules to be in excited states which is relatively less probable. This inelastic scattering gives the information about vibration and rotational modes of materials. Rayleigh scattered lights are filtered out and the inelastic scattered radiations are collected on a detector by passing through a notch filter. Usually Stokes intensity are analysed to obtain the information about the material.

We have used LabRam HR evolution confocal Raman microscope supplied by Horiba for all the Raman measurement of our samples at Solid State Physics Laboratory (SSPL), DRDO, Delhi. It is an achromatic spectrometer which covers the wavelength range from 200-2100 nm by using a special InGaAs detector. The used specifications of Raman measurements of different samples are described in respective chapters.

2.3.7 Photoluminescence (PL)

PL is a non-destructive method to estimate the impurities present in a material along with the band gap information. It generally gives the information about shallow level impurities; however certain radiative deep level impurities can also be investigated using this method. When a light source with energy more than the band gap of material is incident, then electron-hole pairs are created in the sample. After turning the light source off, recombination of electron and holes takes place. Only radiative recombination emits photons which are collected by a detector and a plot is obtained between photon count and the wavelength. Band to band emission is generally dominant at room temperature along with few impurities peak if those are present in the material.

We have used LabRam HR evolution confocal Raman microscope supplied by Horiba (fig. 2.10) for all the PL measurement of our samples at Solid State Physics Laboratory (SSPL), DRDO, Delhi. The used specifications of PL of different samples are described in respective chapters.



Figure 2.10: Camera image of Raman Spectrometer with inbuilt PL spectrometer

2.3.8 Electrical Characterization

We have used Keithley 4200 semiconductor characterization system for current-voltage (I-V) measurements on the samples. The BFO based RRAM samples have been characterized by this system for different analysis in two probe configuration. Autolab Metrohm electrochemical work station equipped with frequency analyser (0.1-10⁵ Hz) is further used for all capacitance-voltage (C-V) measurements and impedance analysis of our samples (figure 2.11). The specifications used for different characterization is explained in the respective chapters of the thesis.



Figure 2.11: Optical image of (a) SCS and (b) Electrochemical workstation, IIT Jodhpur